SANDIA REPORT
SAND2007-6775
Unlimited Release
Printed October 2007

Titanium Cholla: Lightweight, High-Strength Structures for Aerospace Applications

David D. Gill, Clinton J. Atwood, Joshua Robbins, Thomas E. Voth
Peter Dewhurst, David G. Taggart

Prepared by
Sandia National Laboratories
Albuquerque, New Mexico 87185 and Livermore, California 94550

Sandia is a multiprogram laboratory operated by Sandia Corporation,
a Lockheed Martin Company, for the United States Department of Energy's
National Nuclear Security Administration under Contract DE-AC04-94AL85000.

Issued by Sandia National Laboratories, operated for the United States Department of Energy by Sandia Corporation.

Available to DOE and DOE contractors from
U.S. Department of Energy
Office of Scientific and Technical Information
P.O. Box 62
Oak Ridge, TN 37831

Telephone: (865) 576-8401
Facsimile: (865) 576-5728
E-Mail: reports@adonis.osti.gov
Online ordering: http://www.osti.gov/bridge

Available to the public from
U.S. Department of Commerce
National Technical Information Service
5285 Port Royal Rd.
Springfield, VA 22161

Telephone: (800) 553-6847
Facsimile: (703) 605-6900
E-Mail: orders@ntis.fedworld.gov
Online order: http://www.ntis.gov/help/ordermethods.asp?loc=7-4-0#online

SAND2007-6775
Unlimited Release
Printed October 2007

Titanium Cholla: Lightweight, High-Strength Structures for Aerospace Applications

David D. Gill and Clinton J. Atwood
Manufacturing Science and Technology Center
&
Thomas E. Voth and Joshua Robbins
Computation, Computers, Information, and Mathematics Center
Sandia National Laboratories
P.O. Box 5800
Albuquerque, New Mexico 87185-MS1245

Peter Dewhurst and David G. Taggart
University of Rhode Island
College of Engineering
Kingston, RI 02881

Abstract

Aerospace designers seek lightweight, high-strength structures to lower launch weight while creating structures that are capable of withstanding launch loadings. Most "light-weighting" is done through an expensive, time-consuming, iterative method requiring experience and a repeated design/test/redesign sequence until an adequate solution is obtained. Little successful work has been done in the application of generalized 3D optimization due to the difficulty of analytical solutions, the large computational requirements of computerized solutions, and the inability to manufacture many optimized structures with conventional machining processes. The Titanium Cholla LDRD team set out to create generalized 3D optimization routines, a set of analytically optimized 3D structures for testing the solutions, and a method of manufacturing these complex optimized structures. The team developed two new computer optimization solutions: Advanced Topological Optimization (ATO) and FlexFEM, an optimization package utilizing the eXtended Finite Element Method (X-FEM) software for stress analysis. The team also developed several new analytically defined classes of optimized structures. Finally, the team developed a 3D capability for the Laser Engineered Net Shaping™ (LENS®) additive manufacturing process including process planning for 3D optimized structures. This report gives individual examples as well as one generalized example showing the optimized solutions and an optimized metal part.

CONTENTS

FIGURES

TABLES

1. INTRODUCTION

Aerospace applications require light weight, high strength structures to reduce launch weight while withstanding launch and operational loadings. Current methods of "lightweighting" are iterative and time consuming, never actually reaching the optimal structural topology. An example of this is seen in the electrical housing shown in Figure 1. This housing has a rib-on-plate structure to give the side panel of the box sufficient strength at a reduced weight. The means of lightweighting for this housing probably used the knowledge and experience of a designer who selected rib geometry and thickness based on intuition. Finite element method (FEM) analysis software would then have been used to test the structure under load. If the structure passed, there was probably little extra effort to optimize the solution. If the structure failed, the ribs would have been manually adjusted and then retested. In this iterative fashion, a solution would have been achieved for the structural topology of the housing. But the method to achieve results was iterative and knowledge-based, and the results were not optimal.

Figure 1. Aerospace Electrical Housing
Showing Lightweighted Rib-On-Plate Structure.

Topological optimization has been a subject of research since 1904 when Michell introduced optimality criteria [1]. Since that time, there has been further development of 2D structures, but 3D optimization developments have been stifled by the profound complexity of analytical solutions, the overwhelming demands of computing resources for computational solutions, and the lack of manufacturability of many optimized 3D structures. Though the generalized solution has been lacking, several geometry specific optimization packages have been developed for applications such as automobile frames.

The Titanium Cholla LDRD team set out to create a complete capability for generalized 3D topological optimization. The effort included the development of 2 methods of topological optimization using different underlying finite element software. The optimization solutions need to be validated, so the team developed new analytical 3D solutions. In addition, the 2 optimization methods' results were compared for real-life test cases. Finally a 3D manufacturing capability was created to address the manufacturability concerns for topologically optimized structures.

2. ADVANCED TOPOLOGICAL OPTIMIZATION: AN EFFICIENT FINITE ELEMENT BASED TOPOLOGY OPTIMIZATION PROCEDURE FOR THE IDENTIFICATION OF MINIMUM WEIGHT STRUCTURES

The Titanium Cholla team included university partners from the University of Rhode Island. These team members worked on creating a fully 3D capability for Advanced Topological Optimization (ATO), a density modification based method of topological optimization. Additional research by these project partners addressed analytical solutions to 3D optimization problems and their usefulness for verifying the results given by the ATO software. This team wrote 3 papers which will be submitted in the near future. In order to retain full documentation of the results of this research, the papers are included in their entirety in Chapters 2, 3, and 4.

The following paper is titled "An Efficient Finite Element Based Topology Optimization Procedure for the Identification of Minimum Weight Structures" and the authors are David Taggart and Peter Dewhurst of the University of Rhode Island. This paper will be submitted to the journal *Structural and Multidisciplinary Optimization* for publication.

2.1. Background

In the literature, several finite element based topology optimization schemes have been proposed. These schemes can be classified as either material redistribution methods [2, 3] or material removal methods [4, 5]. In the former, a specialized variational principle and material volume constraint equations are utilized, leading to the need for customized finite element codes. For material removal methods a large number of finite element iterations are typically required, and, in some cases, have been shown to fail to provide optimal layouts.

Recently, a new finite element based adaptive topology optimization (ATO) scheme has been developed at the University of Rhode Island. In this procedure, material density is introduced as a nodal field variable that is selectively reduced or enhanced through a series of finite element analyses. This procedure has been shown to converge rapidly to optimal topologies for a variety of test cases where the topologies are known from analytic solutions. Since this scheme can easily be interfaced with existing finite element codes, it provides a robust design tool that can be used to efficiently examine a wide variety of structural optimization problems. In particular, through the development of Fortran user subroutines for use with the commercial Abaqus finite element code [6], users can now easily generate optimal topologies for general structural problems. In the original ATO formulation [7. 8], a material removal scheme was developed. In this scheme, the design domain is taken initially to be fully dense and, after each iteration, the density is gradually reduced in regions of low strain energy. The procedure is applied iteratively until the desired final volume is achieved. While this procedure successfully identified optimal topologies for many test cases, numerous iterations were typically required. After each iteration, the density of only a relatively small number of nodes is adjusted. It was hypothesized that a scheme in which all nodal densities are adjusted at each iteration would provide much faster convergence to the optimal topology. Since the overall goal of the current project is to optimize complex, three dimensional structures, improving the efficiency of the optimization scheme is essential. This report summarizes and demonstrates recent modifications to the original material removal algorithm.

2.2. Finite Element Based Topology Optimization Procedure

In the modified ATO procedure, the desired final mass of the structure is specified at the beginning of the analysis. This material mass is initially distributed uniformly throughout the design domain resulting in a uniform, partially-dense material. All nodes are assigned an initial relative density

$$\rho_o = V_f / V_D \tag{2.1}$$

where V_f is the final structural volume and V_D is the volume of the partially-dense design domain. Since all of the nodes are initially assigned this relative density, the distribution of material densities can be described by the probability distribution function, f_o, given by

$$f_o(\rho) = \delta(\rho - \rho_0) \tag{2.2}$$

where δ is the Dirac delta function and ρ is the relative material density ($0 \le \rho \le 1$). The corresponding cumulative distribution function, F_o, is given by

$$F_o(\rho) = H(\rho - \rho_0) \tag{2.3}$$

where H is the Heaviside step function.

The desired final material distribution is characterized by distinct regions of fully dense material ($\rho = 1$) and regions that have zero relative density. The geometry of the fully dense regions represents the optimized structural topology. For the finite element calculations, a material density of zero would result in zero material stiffness and a singular global stiffness matrix. For these calculations, these regions are assigned a very small relative density, $\rho_{min} << 1$. The resulting final material distribution can be described by the probability distribution function, f_f, given by

$$f_f(\rho) = (1 - \rho_o)\, \delta(\rho - \rho_{\min}) + \rho_o\, \delta(\rho - 1) \tag{2.4}$$

and the corresponding final cumulative distribution is given by

$$F_f(\rho) = (1 - \rho_o)\, H(\rho - \rho_{\min}) + \rho_o\, H(\rho - 1) \tag{2.5}$$

Note that for both the initial and final material distributions, the specified material mass is maintained.

For intermediate iterations, families of probability and cumulative probability distribution functions can be established which provide a smooth transition from the initial distribution (Eqs. 2.2 and 2.3) to the final distributions (Eqs. 2.4 and 2.5). Conditions for the probability distribution function are that all material points have densities between zero and one, leading to the requirement

$$\int_0^1 f(\rho)\, d\rho = 1 \tag{2.6}$$

The requirement that the total mass of material be held constant is satisfied by the condition

$$\int_0^1 \rho\, f(\rho)\, d\rho = \rho_o \tag{2.7}$$

Finally, a scheme is required to incrementally transition from the initial to the final material distribution. These conditions can be met using a family of material distribution functions given by the beta function as

$$f(\rho) = \beta(\rho, r, s) = \frac{\rho^{r-1}\,(1-\rho)^{s-1}}{B(r,s)} \tag{2.8}$$

where r and s are adjustable parameters and

$$B(r,s) = \frac{\Gamma(r)\,\Gamma(s)}{\Gamma(r+s)} \tag{2.9}$$

where Γ is the gamma function. The corresponding cumulative distribution function, also known as the incomplete beta function, is given by

$$F(\rho) = \beta_{inc}(\rho, r, s) = \frac{1}{B(r,s)} \int_0^{\rho} (\rho')^{r-1}\,(1-\rho')^{s-1}\,d\rho' \tag{2.10}$$

This choice of material distribution functions satisfies Eq. 2.6 for any combination of parameters r and s. It can be shown that Eq. 2.7 is satisfied if

$$s = \left(\frac{1-\rho_o}{\rho_o}\right) r \tag{2.11}$$

To provide a smooth transition from the initial to the final material distribution, the following scheme is imposed. If a non-dimensional time parameter, t, is defined such that $t = 0$ corresponds to the initial material distribution and $t = 1$ corresponds to the final material distribution, then we seek values for $r(t)$ that provide a smooth transition over the time interval $0 < t < 1$. This is achieved by determining $r(t)$ such that

$$\int_0^1 \left| \beta_{inc}(\rho', r(t), s) - F_f(\rho') \right| \, d\rho' = 2\,(1-t)\,\rho_o\,(1-\rho_o) \tag{2.12}$$

where F_f is the final cumulative distribution (Eq. 2.5) and $r(t)$ is determined numerically using standard root finding and numerical integration algorithms [9]. Under certain conditions, the root finding algorithm converges slowly and degrades the efficiency of the ATO code. To prevent run time convergence problems of the root finding algorithm, it was recognized that the function $r(t,\rho_o)$ can be established *a priori*. Specific values of $r(t,\rho_o)$ were determined using a Matlab code and are stored using a Fortran DATA statement in the ATO code. During the finite element iterations, a bicubic interpolation algorithm is used to determine the desired values of $r(t,\rho_o)$. Typical material distribution and cumulative distribution curves for the case $\rho_o = 0.3$ are shown in Figure 2 and Figure 3.

At each finite element iteration, the desired $r(t)$ is used to assign nodal densities according to the current density distribution function. The nodal density assignment is performed based on the sorted nodal strain energies computed from the previous iteration. Nodes with relatively low strain energy are assigned reduced nodal densities and nodes with relatively high strain energy are assigned increased nodal densities. Through direct assignment of nodal densities, the desired progression of density distributions is enforced. In computing the element stiffness matrices, the nodal density field is interpolated to give the Young's modulus, E, at each Gauss point according to the relation

$$E = E_d\,\rho \tag{2.13}$$

where E_d is the fully dense Young's modulus. Since the density of each node is reassigned after each finite element iteration, convergence to the final topology can be achieved in relatively few finite element iterations.

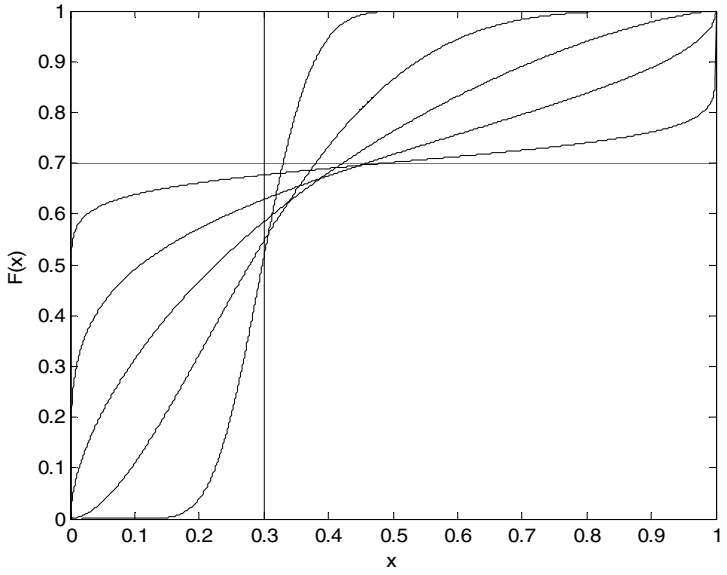

Figure 2. Transition from Initial to Final Probability Distribution.

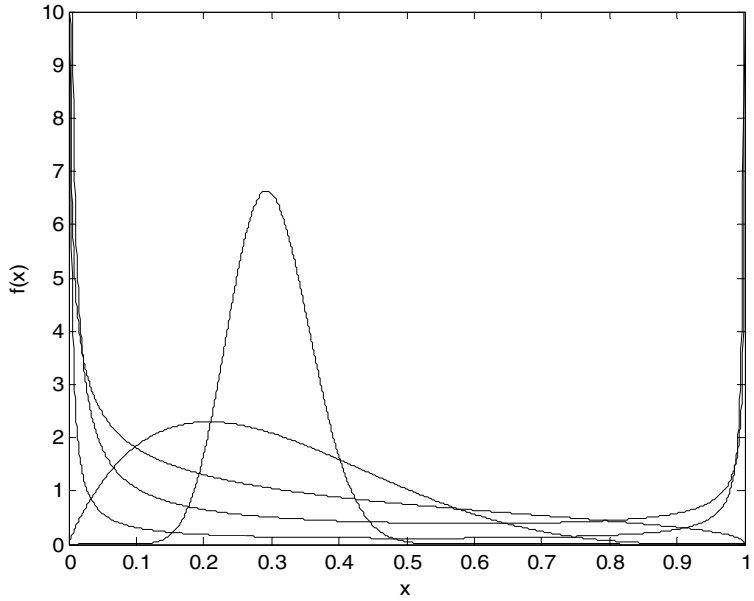

Figure 3. Transition from Initial to Final Cumulative Probability Distribution.

In the material redistribution scheme described above, nodal densities are assigned based on global nodal strain energy distributions with no consideration of the previous density history of a given node. As a result, if too few iterations are performed, numerical instabilities can occur. To avoid such instabilities, a scheme similar to the Euler method for the numerical solution of first order ordinary differential equations is used. In this scheme, the density at node *n* at iteration *i+1* is computed using

$$\rho_{i+1}^{n} = \rho_{i}^{n} + \Delta\rho^{n} \tag{2.14}$$

where $\Delta\rho^n$ is computed from the gradient of ρ^n at iteration *i*. This gradient is estimated by fitting a quadratic interpolation through the points $\rho^n{}_{i-1}$, $\rho^n{}_i$ and $\rho^{n*}{}_{i+1}$ where $\rho^{n*}{}_{i+1}$ is the new nodal density obtained from the strain energy sorting algorithm discussed above. The resulting nodal densities are updated according to

$$\rho_{i+1}^n = \rho_i^n + \frac{\rho_{i+1}^{n*} - \rho_{i-1}^n}{2} \tag{2.15}$$

Through this scheme, stable convergence to the final topology can be achieved with fewer iterations.

2.3. Results and Discussion

The topology optimization scheme based on nodal strain energy sorting has been implemented using the commercial finite element code, Abaqus. The expected advantage of fewer required iterations with convergence to the optimal topology in several 2-D and 3-D test cases has been observed.

2.3.1. Two Dimensional Test Cases

Six test cases as depicted in Figure 4 are considered. Figure 5 shows results for the case of the well known center fan topology first obtained by Michell [1] for the case of a simply supported beam with a single central load (Case 2). For this case, several trials were performed using a design domain with an aspect ratio of 1:1.25, taking advantage of symmetry along the vertical mid-plane. Note that the full model results shown in the figures were generated post-analysis using Abaqus' plug-in tool "Mirror ODB". The trials included two different mesh densities (2,000 elements and 50,000 elements) and three different time step increments (Δt = 0.05, 0.02 and 0.005). The results shown were created using a Pentium 4, 2.60 GHz, with 1.25 GB RAM. As shown in Figure 5, all cases led to comparable topologies. Increasing the mesh density and/or decreasing the step size led to more precise images. These results indicate, however, that the ATO scheme provides reasonable results, even for cases involving coarse meshes and large time steps.

Several other cases were considered to demonstrate that the ATO scheme provides results consistent with known topologies from analytic solutions. For these cases, relatively fine meshes (30,000-70,000 elements) and small time steps (Δt = 0.005) were used. These results for these cases are shown in Figure 6. In cases 1 and 2, the only difference is the boundary condition on the lower right hand node. Changing this boundary condition from a pinned condition to a horizontal roller results in different topologies [1], both of which are correctly identified by the ATO method (see Figure 6a and Figure 6b). Cases 3 and 4 are similar to cases 1 and 2 with the design domain changing from a semi-infinite 2-D space to an infinite 2-D space. Again, the ATO method generates topologies that match the analytic predictions as shown in Figure 6c and Figure 6d. Case 5 is the well known Chan cantilever [10] which again is correctly identified by the ATO method (Figure 6e).

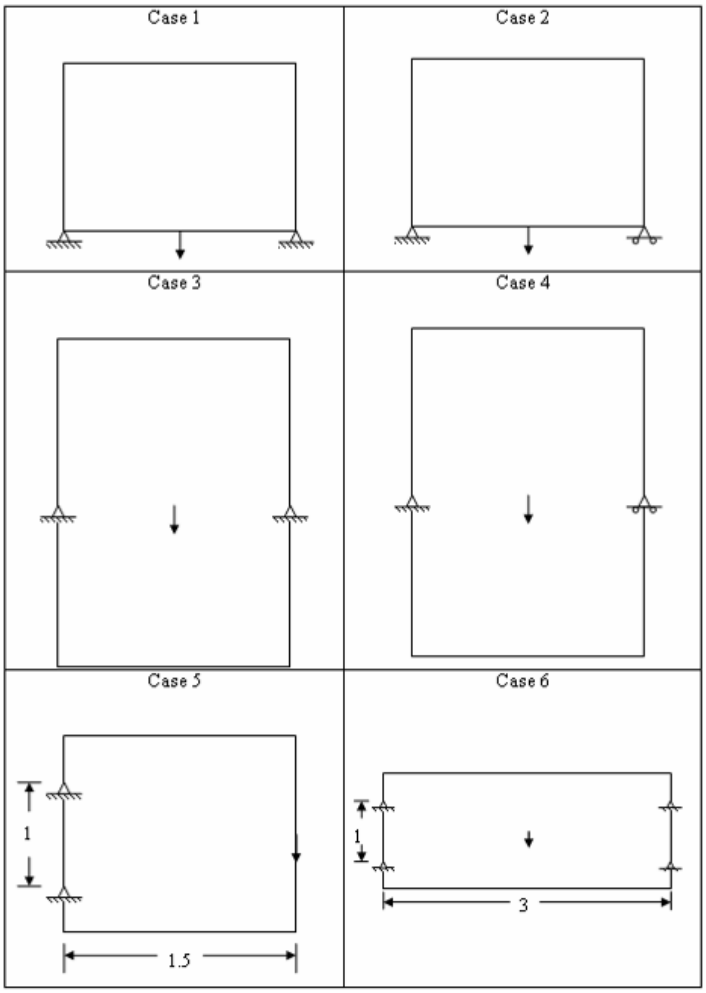

Figure 4. Two Dimensional Test Cases.

The final case considered, Case 6, was motivated by recent correspondence between the project investigators and several international researchers in the field of topology optimization. A solution to this problem proposed in the literature [11] consists of a pair of Chan cantilevers that meet at the center load point. Recently, Dewhurst has shown that solutions obtained by superposition of known optimal topologies are not always valid. For this test case in particular, the solution based on superposition of two Chan cantilevers is not optimal, while that obtained by the ATO method (Figure 6f) does satisfy rigorous optimality criteria. This example clearly demonstrates the ability of the ATO method to identify the correct topologies, even in cases where the optimal topology is not always obvious.

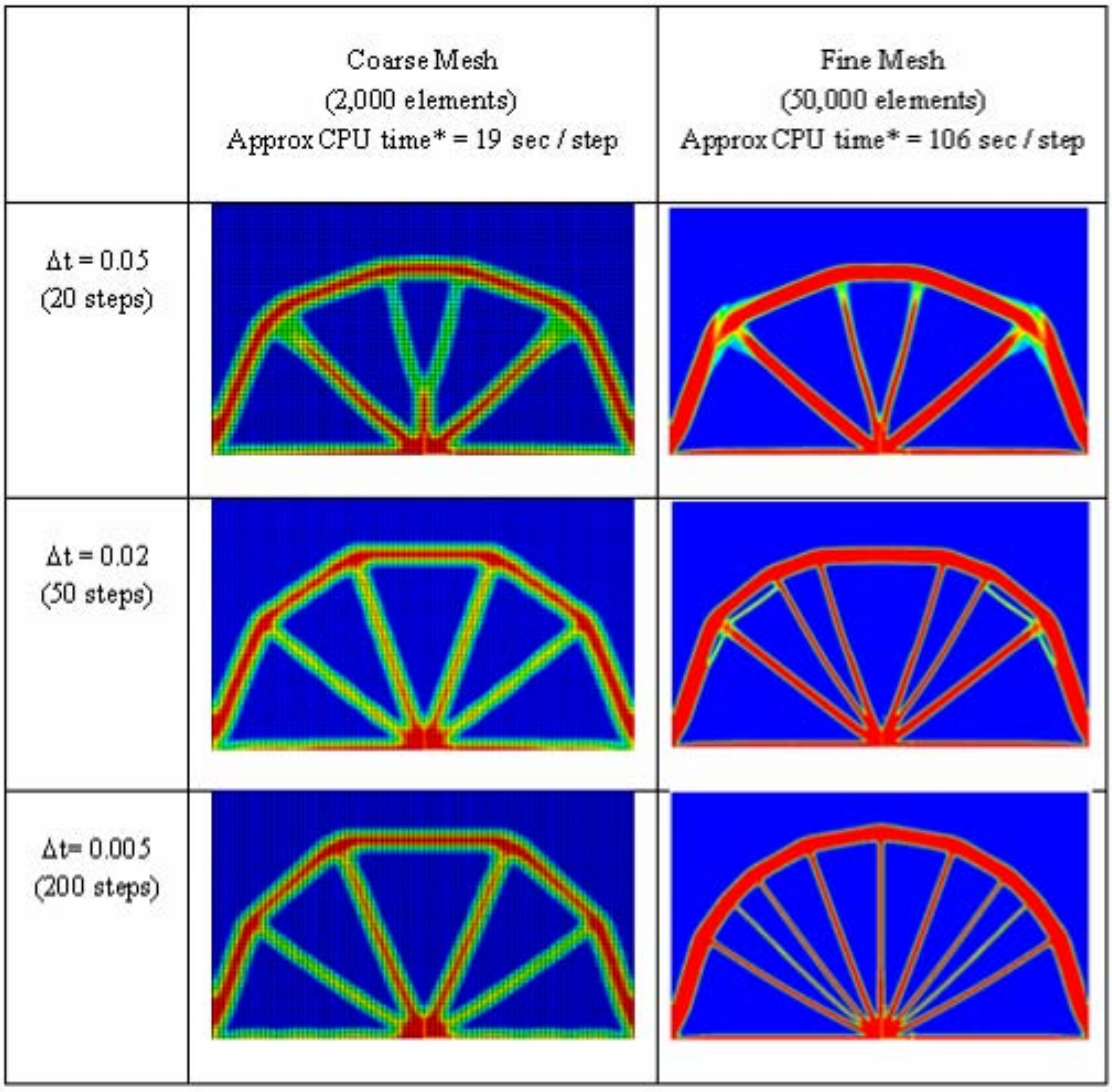

Figure 5. Effect of Mesh Density and Time Increment on Optimal Topology (Case 2).

2.3.2. Three Dimensional Test Case

The method is also extended to 3-D and a sample case is presented that demonstrates the effectiveness of the method in identifying 3-D minimum weight topologies. In this case, element type is an 8 node linear hexahedral (brick) element with reduced integration (the default setting) unselected. Other steps in the analysis procedure are identical to the 2-D procedure. To illustrate the performance of the 3-D ATO method, a test case which is a 3-D generalization of the 2-D Michell center fan topology is investigated. In the 3-D case, a semi-infinite design domain is subjected to a concentrated force normal to the free surface. Support points are equally spaced along a circular region whose center is the load application point. The supports are taken to be roller supports that move only in the radial direction. For this example case, eight support points are defined at increments of $\pi/4$ along the circle. The expected optimal topology for this problem is four Michell center fans as shown in Figure 7.

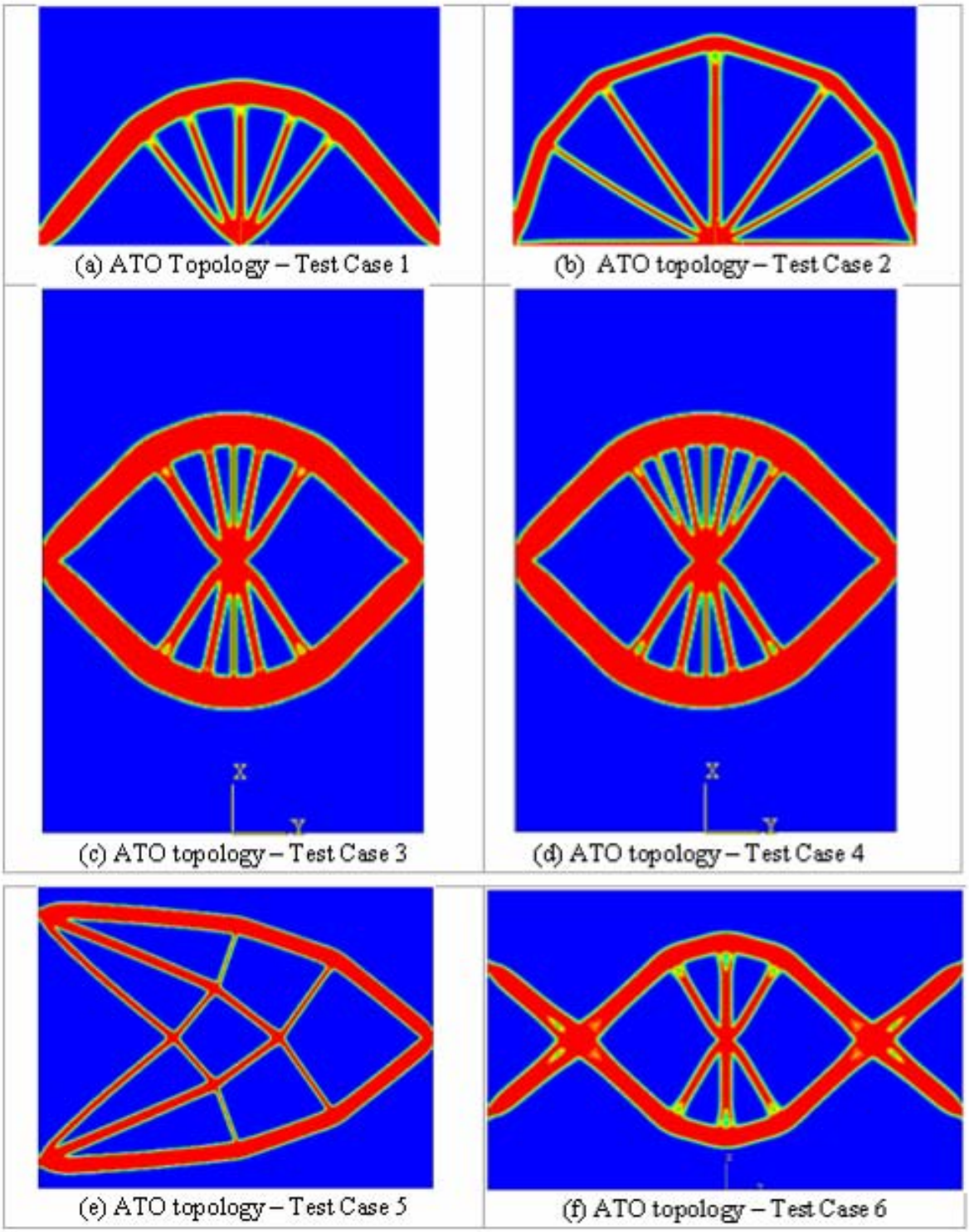

Figure 6. Advanced Topological Optimization Results for Cases 1-6.

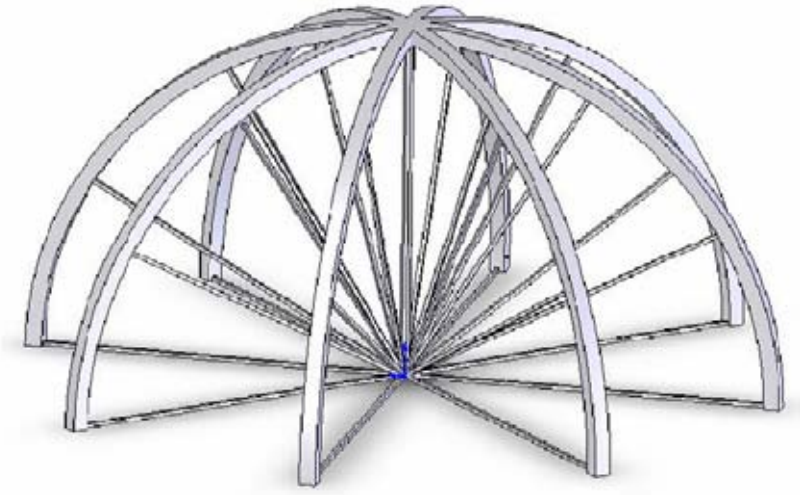

Figure 7. Center Fan Test Case - Expected Topology for a Center-Loaded Structure That Is Simply Supported at 8 Locations.

To model this problem, the design domain is taken to be a cylinder whose radius and height exceed the radius of the support locations. Due to symmetry, the cylindrical domain can be represented by a sector that spans $\pi/8$ of the full cylinder as shown in Figure 8. A quarter symmetry model was created that consisted of a quarter of a circular cylinder. An axial concentrated force is applied at the corner point that represents the center of the full cylinder domain. To model each of the 8 support locations, zero axial and circumferential displacement conditions are imposed at a single point along a radial edge of the domain. Finally, symmetry displacement boundary conditions are imposed along the two symmetry planes such that the model represented one quarter of the actual full cylinder design domain. These load and boundary conditions are illustrated in Figure 8.

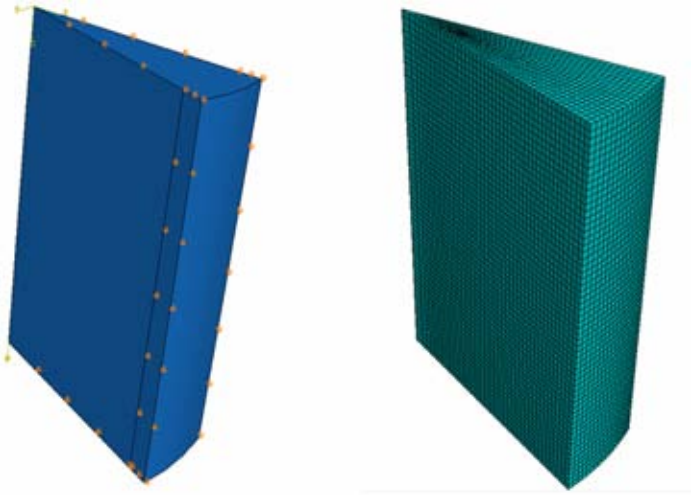

Figure 8. 3D Model Showing Loads and Boundary Conditions (left) and Meshed Model (right).

The region was meshed using 41,040 linear hexahedral (8-node) elements as shown in Figure 8. The results of the ATO consist of nodal densities where nodes are either nearly fully dense ($\rho=1$) or have essentially zero density ($\rho<\rho_{min}$). Visualization of the final topology is achieved by generating 3-D surfaces corresponding to the surface of the fully dense regions. Software has been developed that implements the marching cube algorithm to generate triangulated surfaces that are stored in standard STL CAD format. The resulting file can viewed in numerous commercial CAD packages. The resulting structure for this test case is shown in Figure 9. It is clear that this topology corresponds very well with the expected topology (Figure 7).

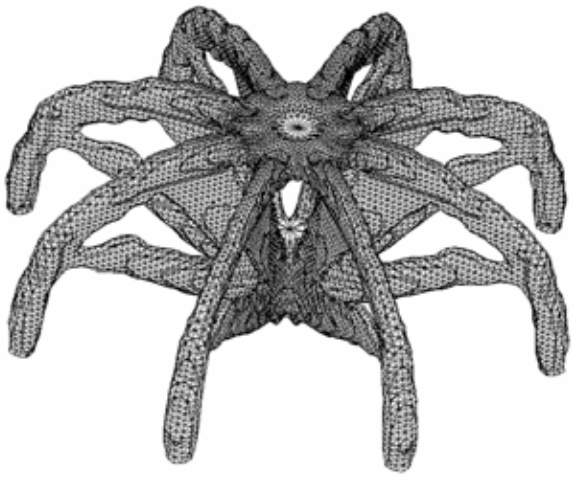

Figure 9. ATO Results for Center Loaded Fan Structure.

2.4. Conclusions

A novel finite element topology optimization procedure is presented. This procedure is shown to identify minimum-weight topologies for several 2-D and 3-D problems for which the optimal topology is known from classical theoretical solutions. The method is shown to be effective even for coarse finite element meshes and relatively few finite element iterations. Hence, it is believed that this scheme provides an efficient method for identifying optimal topologies for complex design problems. Also, since the scheme can be implemented in commercial finite element codes that provide the capability for user defined subroutines, application to general design problems is simplified due to robust user interface tools for both problem definition and visualization of final results.

3. ABSOLUTE MINIMUM WEIGHT STRUCTURES FOR COMBINED TORSIONAL AND AXIAL LOADING

In addition to the development work completed on the Advanced Topological Optimization (ATO) method, the Titanium Cholla team members from the University of Rhode Island also worked to develop new analytical optimization solutions. The purpose of the analytical solutions was to develop test structures for use in verification of ATO results. The paper included in this chapter records the efforts of the team to create minimum weight structures for combined axial and torsional loading. This paper will be submitted to the journal *Structural and Multidisciplinary Optimization* and was authored by Peter Dewhurst and David G. Taggart.

3.1. Introduction

Interest in Michell [1] structures has increased in recent years mainly because of the development of numerical structural optimization methods, for which the determination of the optimal structural layout is the core problem. Known Michell solutions and their properties serve as valuable test cases for these numerical optimization methods. Up to the present time most of the work with both Michell structures and numerical optimization has been two-dimensional. The only non-trivial minimum-weight structure remains the spherical loxodrome solution, for pure torsion, given in Michell's original paper. Michell conjectured that the loxodromes on all spherical surfaces, concentric to the proposed structure surface, would be uniformly and equally extended or compressed, and so subjected to constant strain magnitude. Any structure that deviates from the loxodrome directions on the solution sphere, or deviates inside or outside of the sphere, must thus follow directions subjected to less strain magnitude, and so violates the requirements for optimality; see Michell [1], Hemp [12], Prager [13], Rozvany [14], Dewhurst [15]. Lewinski [16] has established the global optimality of Michell's loxodrome structure using classical calculus of variations. In the present paper an alternative proof of optimality is given, by posing the problem as one in variational calculus, which has an obvious constant radius solution.

In the present work, the more general problem is considered of determining the topology of minimum-weight axially-symmetric structures, subjected to both torsional and axial loading. In the early sections of the paper, the family of structures, confined to a cylindrical surface, are considered. It is shown that, in the this case, the optimal solution is one where the structural members follow two families of complimentary helices; one family at angle γ to the cylindrical axis, and the complimentary family at angle $\pi/2-\gamma$. For a given ratio of torsional to axial loading, the precise angle γ will be shown to be defined by the requirement of radial equilibrium. The results of numerical topological optimization studies, are shown at the end of the paper to be in complete agreement with the theoretically derived values.

Following analyses of the cylindrical structures, the application of both torsional and axial loading, to spherical loxodrome structures, is considered. As for the cylindrical structures, the general result is shown to follow the two families of complimentary loxodromes, inclined angles γ and $\pi/2-\gamma$ to meridians, and defined by the requirement of radial equilibrium.
Finally a comparison of the cylindrical and spherical structures for varying ratios of axial to torsional loading shows, as expected that as the torsional load component tends to zero, the

optimal solution is given by a cylindrical structure where the helix angle has tended to zero; i.e. the solution tends to a set of columns or tie rods arranged around a pitch circle. Alternatively, as the axial component tends to zero, the solution tends to Michell's solution, following the $\pm\pi/4$ loxodrome families. Between these two limits, global optimally-optimal spiral solutions clearly exist around axially-symmetric envelopes, which range between the cylindrical and spiral limits. The general shape of these intermediate solutions may be uncovered through appropriate numerical topological optimization.

The analyses presented in this paper are restricted to the condition of equal material strength in tension and compression. If this condition does not apply, then the value of the spiral angle γ must be chosen to satisfy the strain conditions around the loading circles; see Hemp [17], and Rosvany [14]. The additional condition for radial equilibrium then gives rise to the need for radial members.

3.2. General Cylindrical Helical Structures

In pure torsion of a cylinder the lines of maximum and minimum strain follow opposite families of 45-degree helices. The truss structure formed by placing nodes, at constant angular increments along these helices, whose connecting members are equal helical chords, thus satisfies all of the requirements of a least-weight Michell structure. A rapid prototyped example of such a structure is shown in Figure 10.

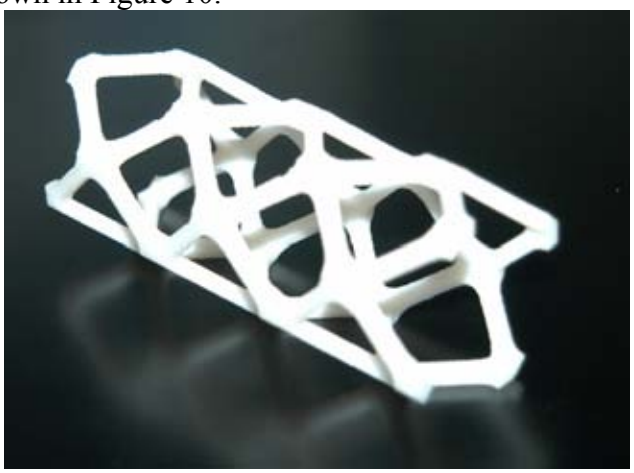

Figure 10. Pure Torsion Cylindrical Structure.

In this case nodes are positioned at 45-degree angular increments around the cylinder. Pure torsion introduces the same force magnitude into the tension and compression members, and the symmetry of the members surrounding each node ensures that the structure is in equilibrium. In particular the radially inward component of the two tension members at each node is cancelled by the radially outward component of the two compression members. If an axial load is introduced in addition to the torsion load, then tension and compression members will carry different internal forces and radial equilibrium can no longer be assumed. The general requirement for radial equilibrium will be examined next.

3.2.1. Conditions for Radial Equilibrium

The combination of axial and torsional loading gives rise to principal strain directions which follow two orthogonal families of opposite equi-angular helices. Below we will examine this

more general strain field to determine the conditions for equilibrium with arbitrary ratios of axial to torsional loading.

Consider two families of equi-angular helices; left-hand α helices intersecting the axial direction at constant angle γ, and right-hand β helices intersecting the axial direction at constant angle $(\pi/2-\gamma)$. It can be shown that the α helices are represented by the parametric equations

$$\begin{aligned} x &= r\cos(\theta) \\ y &= -r\sin(\theta) \\ z &= r\cot(\gamma)\theta \end{aligned} \qquad (3.1)$$

and the β helices by

$$\begin{aligned} x &= r\cos(\theta') \\ y &= r\sin(\theta') \\ z &= r\tan(\gamma)\theta' \end{aligned} \qquad (3.2)$$

where θ and θ' are angles of rotation about the z-axis measured counterclockwise and clockwise respectively from the x-axis. Without loss of generality the α helices will be taken as the layout lines for the tension members and the β helices will lay out the compression ones. Figure 11 illustrates the helical network produced by the two helical families for the case $\gamma=\pi/6$.

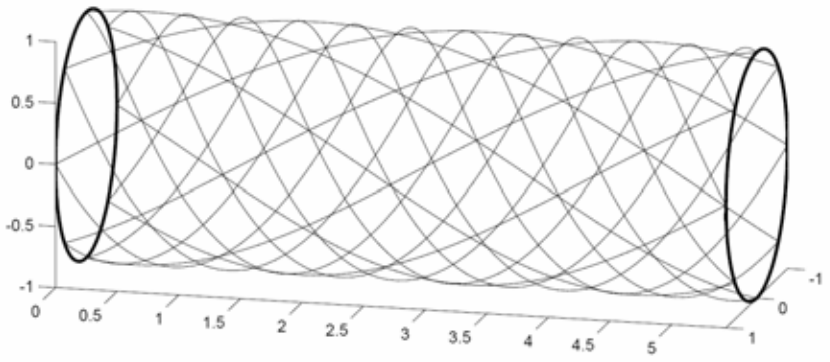

Figure 11. Strain Field for Axial and Torsional Loading ($\gamma=\pi/6$).

To establish the relationship between θ and θ' between the nodes of the helical network we can note that they involve equal separation in the axial direction (z) along the two families. Thus from (3.1) and (3.2)

$$r\cot(\gamma)\theta = r\tan(\gamma)\theta' \quad \text{or} \quad \theta' = \cot^2(\gamma)\theta \qquad (3.3)$$

Michell structures may be considered as truss structures with closely spaced nodes so the discrete members follow as closely as possible the curvilinear optimal strain field. For the present case we will consider the nodes to be separated by constant parameter increments $\Delta\theta$ and $\Delta\theta'$ respectively. The members connected to an arbitrarily selected node, taken as a local origin, thus have co-ordinate lengths given by Eqs. (3.1) and (3.2) as

$$\Delta x = r\Delta\theta^2/2$$
$$\Delta y = r\Delta\theta \qquad (3.4)$$
$$\Delta z = r\cot(\gamma)\Delta\theta$$
$$\Delta x = r\Delta\theta'^2/2$$
$$\Delta y = r\Delta\theta' \qquad (3.5)$$
$$\Delta z = r\tan(\gamma)\Delta\theta'$$

for the tension and compression members respectively. Assume the tension members carry internal force f_T and the compression members force f_C. Equations (3.4) and (3.5) show that the tension and compression members are orthogonal in the y-z plane to order $\Delta\theta^2$, and so equilibrium in the y and z directions is assured. It therefore only remains to establish equilibrium in the x-direction. From Eqs.(3.4), the component of tensile force f_T in the x-direction is given by

$$f_{Tx} = f_T\left[\frac{\Delta\theta}{2(1+\cot^2(\gamma))^{1/2}}\right] \qquad (6)$$

where the term in brackets is the x-component of the unit vector along the tensile member. Similarly from Eqs.(3.5) the x-component of compressive force f_C is

$$f_{Cx} = f_C\left[\frac{\Delta\theta'}{2(1+\tan^2(\gamma))^{1/2}}\right] \qquad (7)$$

and substituting for θ' from Eq.(3.3) gives

$$f_{Cx} = f_C\left[\frac{\cot^2(\gamma)\Delta\theta}{2(1+\tan^2(\gamma))^{1/2}}\right] \qquad (8)$$

Substituting Eqs.(3.6) and (3.8) into the required condition $f_{Tx} = f_{Cx}$ gives after some trigonometric manipulation

$$f_C = \tan^3(\gamma)f_T \qquad (9)$$

Equilibrium condition (3.9) can be established in a more insightful way by obtaining first the rotation along the orthogonal helical paths. The radii of curvature of the α and β helices are given by

$$R_\alpha = r(1+\cot^2(\gamma)), R_\beta = r(1+\tan^2(\gamma)) \qquad (10)$$

Consider a right elemental triangle on the cylinder surface with sides length $r\Delta\theta$ in the circumferential and $r\cot(\gamma)\Delta\theta$ in the axial directions. The hypotenuse is then equal to $R_\alpha\Delta\alpha$ in the direction of the α helix, where $\Delta\alpha$ is the angle turned through along the helical path. From Pythagoras this yields

$$\Delta\alpha = \Delta\theta/(1+\cot^2(\gamma))^{1/2} = \Delta\theta\sin(\gamma) \qquad (11)$$

and similarly

$$\Delta\beta = \Delta\theta'/(1+\tan^2(\gamma))^{1/2} = \Delta\theta'\cos(\gamma) \qquad (12)$$

The requirement for radial equilibrium, using the small angle approximation for sine, can now by written as

$$f_T\Delta\alpha = f_C\Delta\beta \qquad (13)$$

And substituting for $\Delta\alpha$, $\Delta\beta$ and θ' from Eqs.(11), (12) and (3) yields equilibrium condition (3.9) as required.

3.2.2. Internal Forces in the Structural Members

A necessary step to establish the truss volume is to relate the equilibrium condition, and the axial and torsional loads imposed on the structure, to the internal forces in the structural members. Figure 12 shows the axial and shear force components imposed on a single node from the external loading. Applying axial and circumferential equilibrium conditions on the node, and substituting for f_C from radial equilibrium condition (3.9) gives

$$\begin{aligned} f_n &= f_T(\cos(\gamma) - \sin^4(\gamma)/\cos^3(\gamma)) \\ f_t &= f_T(\sin(\gamma) + \sin^3(\gamma)/\cos^2(\gamma)) \end{aligned} \tag{3.14}$$

Dividing Eqs.(3.14) and simplifying leads to the elegant result

$$\gamma = \cot^{-1}((f_n/f_t)/2)/2 = \cot^{-1}(\cot(\eta)/2)/2 \tag{3.15}$$

where η is the angle of the resultant force; see Figure 12

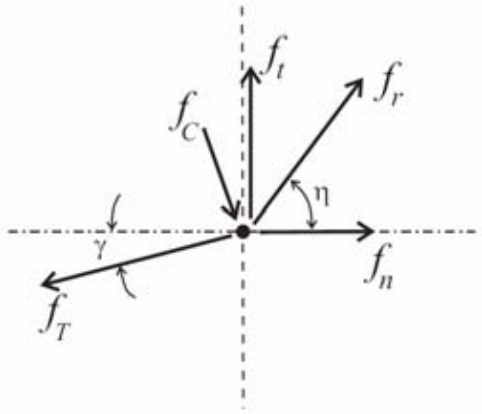

Figure 12. Forces Acting on a Node.

This result ranges from $\gamma = \pi/4$ for $f_n=0$ (pure torsion) to $\gamma = 0$ for $f_t=0$ (pure axial loading. For the latter, the structure has become simply a set of axial members at angular spacing $\Delta\theta$ on a pitch circle of radius *r*. Note also at this point Eq.(3.9) predicts $f_C = 0$ consistent with the circular column limiting solution.

In terms of the global loading on the structure, the axial force *F* and torque *T* are represented by

$$\begin{aligned} F &= \frac{2\pi}{\Delta\phi} f_n \\ T &= \frac{2\pi r}{\Delta\phi} f_t \end{aligned} \tag{3.16}$$

Where $\Delta\phi = \Delta\theta + \Delta\theta'$ is the angular spacing of nodes around the cylinder.

Thus for any arbitrary combination of axial load *F* and torque *T*, the optimal cylindrical structure layout comprises orthogonal families of helices intersecting the axial direction at angles γ and $(\pi/2 - \gamma)$ respectively, where

$$\gamma = \cot^{-1}((Fr/T)/2)/2 \tag{3.17}$$

The results in the last two sub-sections can now be used to establish analytical expressions for the volume of the tension and compression members in the general helical structure.

3.2.3. Volume Calculations

To obtain an analytical expression for volume it is necessary to express the loading in terms of the resultant force f_r acting on each node (see Figure 12) and the sum of these forces for all of the nodes at the end faces (and any other cross section), which will be represented by symbol F_r. F_r thus represents the magnitude of the total force distribution at on any normal cross-section of the structure and is given by

$$F_r = f_r(2\pi/\Delta\phi) \tag{3.18}$$

Taking the resultant of the two force components in Eq.(3.14) gives, after simplification of the trigonometric terms

$$f_r = f_T(1+\tan^6(\gamma)) = f_C(1+\cot^6(\gamma)) \tag{3.19}$$

The volume of a single tensile element can now be expressed as

$$\Delta V_T = \Delta l_T f_T/\sigma \tag{3.20}$$

Where σ is the limiting tensile stress value (assumed equal in tension and compression), and Δl_T is the length of the tensile elements which can represented by

$$\Delta l_T = \Delta z/\cos(\gamma) \tag{3.21}$$

where Δz is the axial distance between adjacent circles of nodes as given in Eq.(3.4). Making substitutions into Eq.(3.20) for f_T, Δl_T from Eqs.(3.19) and (3.21), replacing f_r with F_r from Eq.(3.18), and taking the limit as $\Delta\phi$, Δz and ΔV_T tend to zero gives the expression for the total volume of tensile elements as

$$V_T = \frac{F_r}{2\pi\sigma\cos(\gamma)(1+\tan^6(\gamma))^{1/2}}\int_0^L\int_0^{2\pi} d\phi dz = \frac{F_r L}{\sigma\cos(\gamma)(1+\tan^6(\gamma))^{1/2}} \tag{3.22}$$

where L is the length of the cylindrical structure. Similarly it can be established that the volume of the compression elements is

$$V_C = \frac{F_r}{2\pi\sigma\sin(\gamma)(1+\cot^6(\gamma))^{1/2}}\int_0^L\int_0^{2\pi} d\phi dz = \frac{F_r L}{\sigma\sin(\gamma)(1+\cot^6(\gamma))^{1/2}} \tag{3.23}$$

V_T, V_C and their sum (total structure volume) can be compared using dimensionless volume given by $V^* = V/(F_r L/\sigma)$.

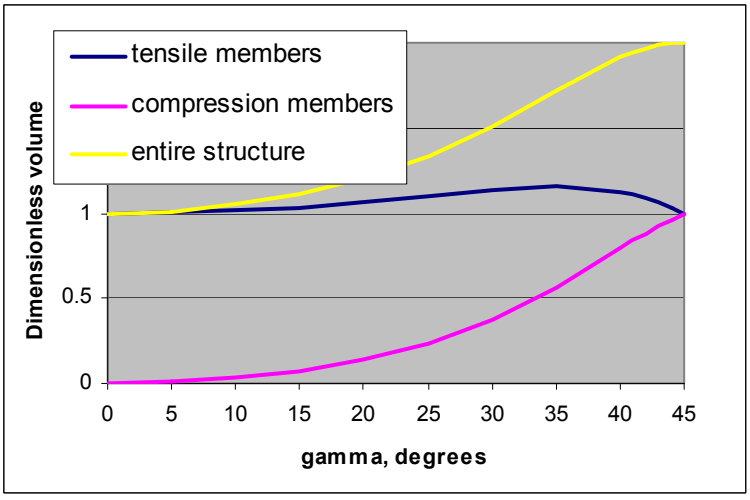

Figure 13. Relationship Between Helix Angle and Dimensionless Volume.

It can readily be verified that the dimensionless volume for pure axial load should be 1.0 and for pure torsion 2.0 as predicted by Eqs.(3.22) and (3.23). For a check of the intermediate volume values it is necessary to change the volume equations to functions of resultant force angle η; see Figure 12. From Eq.(3.15) we can write

$$\eta = \cot^{-1}(2\cot(2\gamma)) \tag{3.24}$$

Equations (3.22), (3.23) and (3.24) provide the plot of dimensionless volume against resultant force angle η shown in Figure 14. If a tube with yield stress value σ is subjected to a distributed load of total magnitude F_r at angle η to the axial direction, then using Tresca's yield criterion the minimum volume is given by

$$V_{tube} = \frac{2F_r L}{\sigma}\left[\frac{\cos^2(\eta)}{4} + \sin^2(\eta)\right]^{1/2} \tag{3.25}$$

It can readily be shown that this results is numerically equal to the structure volume given by Eqs.(3.22), (3.23) and (3.24); i.e. Eq.(3.25) gives precisely the total volume relationship in Figure 14. This validates the analyses above since a tube is clearly a perfectly efficient geometry for support of the cylindrically symmetric loading. The use of Tresca's yield criterion provides this validation since it predicts constant strain energy levels equivalent to those in the truss structure. Analytical transformation of Eqs.(3.22), (3.23) and (3.24) into Eq.(3.25) has remained elusive up to this point.

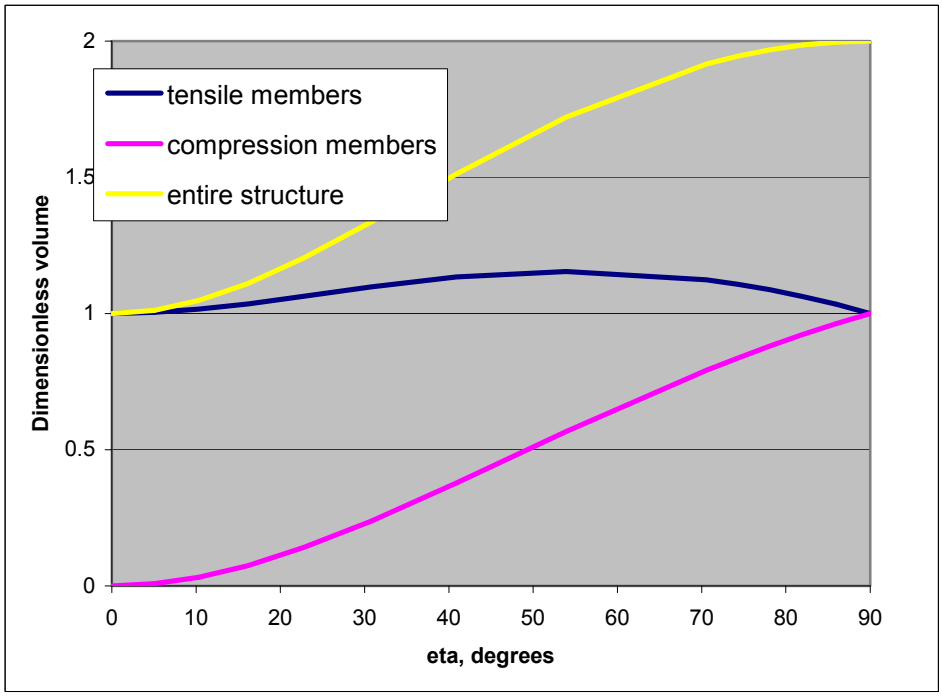

Figure 14. Relationship Between Resultant Force Angle and Dimensionless Volume.

3.3. Alternative 'Cylindrical' Structural Forms

As an alternative to structures formed on the cylindrical surface and designed to be in equilibrium, we could propose truly 3-dimensional cylindrical structures which include members

in the radial direction from each node. An interesting case to consider is one analogous to problem of supporting a force offset from a support surface; see Figure 15.

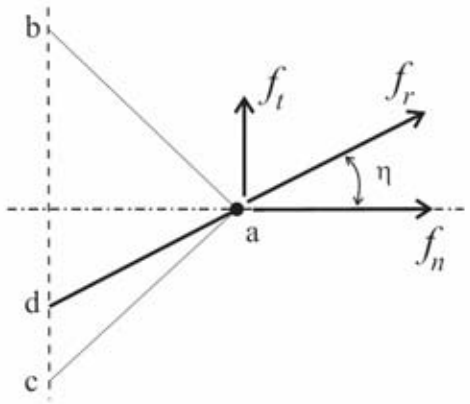

Figure 15. Support of Force from Offset Surface

In this case if the angle of the resultant force η is greater than $\pi/4$, then the optimal support structure is an orthogonal 2-bar truss lying along layout lines *ba* and *ca*. However, if η is less than or equal to $\pi/4$, then the optimal structure changes to a single member (tie-bar or column depending on the direction of f_r). By analogy one could imagine a cylindrical structure comprising 45 degree helices if the resultant perimeter force angle η is greater than $\pi/4$, and becoming a single family of helices aligned with the resultant perimeter forces if η is less than or equal to $\pi/4$; in both cases including radial members from each node to provide radial equilibrium. This would satisfy the optimality requirement for the members to be laid out along the maximum strain directions of a candidate virtual strain field. However, it is also required for the strain in all three principal directions to have equal strain magnitude ε and for this to be compatible with the kinematic displacements of the structure. In this case for the radial direction to be subjected to strain magnitude ε, requires that the circumferential direction also experiences the same strain magnitude. This cannot be the case since on the cylindrical surface the maximum strain directions are at angles γ and $(\pi/2-\gamma)$ to the circumferential direction. Thus it can be concluded that such structures would not be optimal. As a check on this conclusion, the volume of a single helix family and supporting radial members is evaluated below.

Figure 16 shows a single helix for the case $\eta=\gamma=\pi/4$, which is assumed to be subjected to force f_r at the ends, and which is therefore propagated along its length. The radial members are separated by constant spacing Δz along the axis. The volume of the elements along this single helix is thus given by

$$\Delta V_T = \Delta l_T f_r/\sigma = \frac{\Delta z}{\cos(\gamma)}\frac{F_r\Delta\phi}{2\pi}/\sigma \tag{3.26}$$

and so the total volume of the helical elements is

$$V_T = \frac{F_r}{2\pi\sigma\cos(\gamma)}\int_0^L\int_0^{2\pi} d\phi dz = \frac{F_r L}{\sigma\cos(\gamma)} \tag{3.27}$$

The radial members must provide radial equilibrium and so with reference to Eqs.(3.13), (3.11) and (3.4) we may write the compressive force, f_C, in the radial members as

$$f_C = f_T \Delta\alpha = f_r \Delta\theta \sin(\gamma) = \frac{f_r \Delta z \sin(\gamma)}{r \cot(\gamma)} \tag{3.28}$$

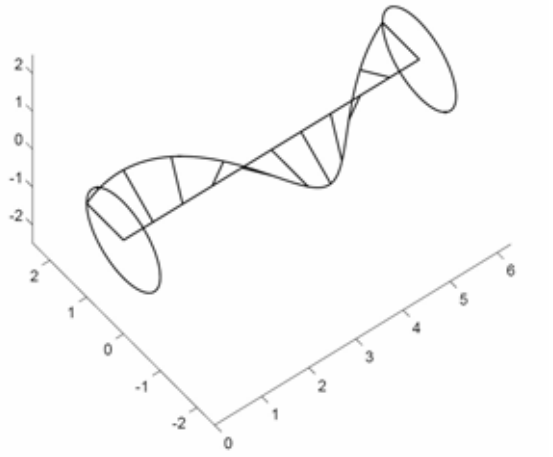

Figure 16. Single Radially Supported Helix.

Thus the volume of a single radial member can be expressed as

$$\Delta V_C = f_C / \sigma = \frac{F_r \Delta\phi}{2\pi\sigma} \frac{\Delta z \sin^2(\gamma)}{\cos(\gamma)} \tag{3.29}$$

In the limit, Eq.(3.29) integrates to give the total volume of all the radial members as

$$V_C = \frac{F_r L}{\sigma} \frac{\sin^2(\gamma)}{\cos(\gamma)} \tag{3.30}$$

The volume of the single-family helix structure is plotted against the corresponding minimum-weight double helix structure in Figure 17. It can be seen that the volume of the structure with radial members is everywhere larger than the cylindrical surface structure, as predicted by the optimality criterion.

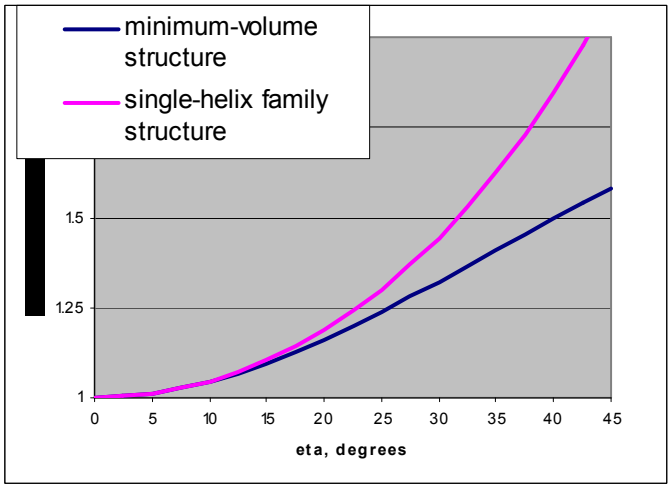

Figure 17. Comparison of Single-Helix Structure with Corresponding Minimum-Weight, Double Helix Structure.

3.4. General Loxodrome Structures

Figure 18 shows the structural layout of complimentary loxodromes or spherical spirals. This is a generalization of Michell's proposed solution, for the transmission of a pure moment between concentric offset circles, comprising two families of 45-degrees loxodromes around the spherical surface connecting the two torsion drive circles. These layout lines are less familiar today that at the time of the Michell paper when they were still used extensively for navigation on the earth's surface. Following an appropriate constant compass heading, or a so called rhumb line, could provide a reasonable approximation to a great circle route for ocean voyages remote from the poles. The actual course followed would be along a constant angle loxodrome which would spiral in towards the pole if followed large distances from the equator.

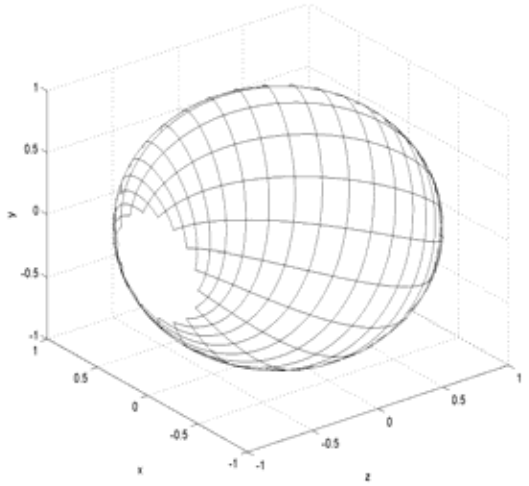

Figure 18. λ=[2,-1/2] or γ=[60˚, -30˚] Complimentary Loxodromes.

Loxodromes are represented by the set of parametric equations

$$\begin{aligned} x &= R\cos(\phi)\sec h(\lambda\phi) \\ y &= R\sin(\phi)\sec h(\lambda\phi) \\ z &= R\tanh(\lambda\phi) \end{aligned} \tag{3.31}$$

where λ is the constant slope of the loxodrome curves with circles of latitude, and parameter ϕ represents the magnitude of the angle turned through about the spherical axis. The layout in Figure 18 shows a family of right-hand loxodromes for which $\lambda = 2$, and the family of complimentary left-hand loxodromes for which $\lambda = -1/2$.

The problem to be addressed in this section of the paper is the determination of the angle of families of loxodromes which will provide an equilibrium structure subjected to an arbitrary combination of axial and torsional loading. The purpose of this analysis is to show that a general loxodrome structure is more efficient than a general helical structure, for carrying both axial and torsional loads when the torsional component is the dominant loading; and vice versa. This will illustrate the need for intermediate, axially symmetric layouts if globally optimal structures are to be obtained. It should be noted that in order to subject a barrel-shaped, or spherical structure, to

an axial loading component it is necessary to include rings or collars to carry the radial reaction-force components from the structural elements. These elements will be considered part of the bearing and support system, and will not be included as part to the structural weight.

The forces transmitted to each node attached to the collar will be f_n and f_t as shown in Figure 12. In this case f_n will be in plane of the spherical structure as illustrated in an axial section through the structure in Figure 19. The value of f_n varies with latitude angle θ according to

$$f_n = f_z / \sin(\theta) = F(\Delta\phi / 2\pi) / \sin(\theta) \tag{3.32}$$

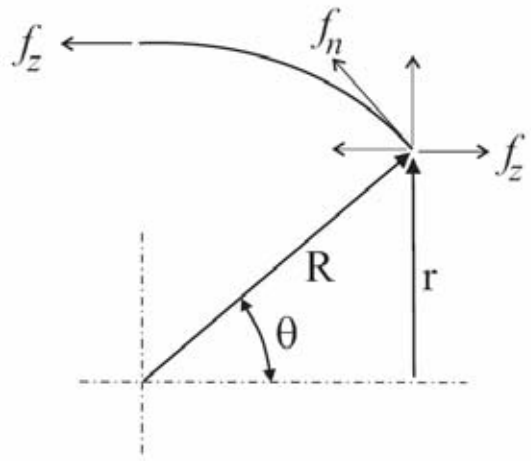

Figure 19. Section Through Sphere Subjected to Axial Loading.

where f_z is the constant axial force component at each node, F is the axial load on the structure and $\Delta\phi$ is the angular spacing between the nodes around any latitude circle. Thus from Eq.(3.11) it can be seen that

$$f_n r = F(\Delta\phi / 2\pi) R = constant \tag{3.33}$$

But the tangential force component f_t is related to the applied torque T by

$$f_t r = T(\Delta\phi / 2\pi) = constant \tag{3.34}$$

Thus from Eqs.(3.33) and (3.34) the ratio of f_n to f_t has constant value given by

$$f_n / f_t = FR / T \tag{3.35}$$

It now remains to be shown that this result leads to a constant angle of intersection of for the layout of an equilibrium structure, which would in turn show that the layout follows the required loxodrome layout.

Consider a local Cartesian co-ordinate system (x', y', z') at one of the nodes of a structure, laid out along two families of complimentary loxodromes, as shown in Figure 19. Consider a tensile element of the structure, carrying force f_T following a loxodrome of slope λ and spanning spherical co-ordinate angles $\Delta\theta, \Delta\phi$.

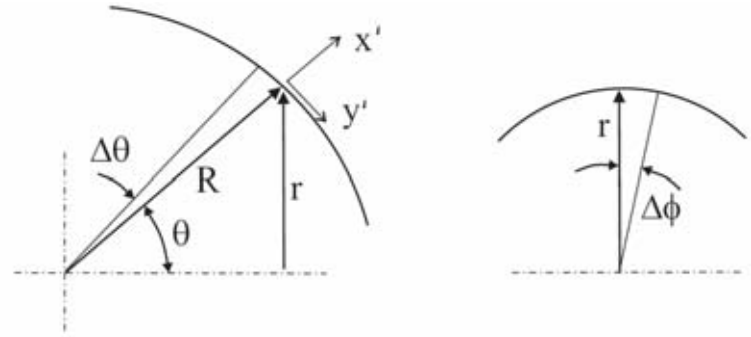

Figure 20. Local Coordinate System at Node on Latitude Circle Radius r.

The length of the element is given by

$$\Delta l_T = R(\Delta\theta^2 + \Delta\phi^2 \sin^2(\theta))^{1/2} \tag{3.36}$$

and since loxodrome slope $\lambda = \Delta\theta/(\sin(\theta)\Delta\phi)$ Eq. 3.36 can be simplified to

$$\Delta l_T = R\sin(\theta)\Delta\theta(1+\lambda^2)^{1/2} \tag{3.37}$$

The displacement along the element has x' component given by

$$\Delta x' = R(1-\cos(\Delta\theta)) + r(1-\cos(\Delta\phi))\sin(\theta) \tag{3.38}$$

And since slope λ equals $R\Delta\theta/(R\sin(\theta)\Delta\phi)$ this can be simplified to

$$\Delta x' = R(\Delta\theta^2/2)(1+1/\lambda^2) \tag{3.39}$$

The component of tensile force f_T in the x-direction is thus given by

$$f_{Tx} = f_T[(\Delta\theta/2)(1+1/\lambda^2)^{1/2}] \tag{3.40}$$

where the term in brackets is the x'-component of the unit vector along the tensile member.

Similarly it can be shown that the x'-component of the compressive force f_C, carried by a compression element following the complimentary loxodrome with slope magnitude $1/\lambda$ is

$$f_{Cx} = f_C(\Delta\theta/2)(1+\lambda^2)^{1/2} \tag{3.41}$$

From Eqs.(3.36) and (3.37), for an equilibrium structure we require

$$f_T(1+\lambda^2)^{1/2} = f_C(1+1/\lambda^2)^{1/2} \tag{3.42}$$

which simplifies to

$$f_C = f_T\tan(\gamma) \tag{3.43}$$

Applying equilibrium for any node in the x' and z' (see Figure 12) and substituting for f_C from Eq.(3.43) gives

$$\begin{aligned} f_n &= f_T(\cos(\gamma) - \sin^2(\gamma)/\cos(\gamma)) \\ f_t &= 2f_T\sin(\gamma) \end{aligned} \tag{3.44}$$

Taking the quotient of Eqs.(3.44) and simplifying gives

$$\gamma = \cot^{-1}(f_n/f_t)/2 \tag{3.45}$$

And substituting $f_n / f_t = \cot(\eta)$ from Figure 12 gives

$$\eta = 2\gamma \tag{3.46}$$

Taking the resultant, f_r, of the two force components in Eq.(3.44) and simplifying gives

$$f_r = f_T / \cos(\gamma) \tag{3.47}$$

or alternatively from Eq.(3.43),

$$f_r = f_C / \sin(\gamma) \tag{3.48}$$

3.4.1. Volume Calculations

We may define the global loading on the structure by parameter *G* given by

$$G = (f_r r)(2\pi / \Delta\phi) = (2\pi / \Delta\phi) r (f_n^2 + f_t^2)^{1/2} = (T^2 + (FR)^2)^{1/2} \tag{3.49}$$

From Eqs.(3.37) and (3.47) the volume of a tensile loxodrome truss element is

$$\Delta V_T = R\Delta\theta(1 + 1/\lambda^2)^{1/2} f_r \cos(\gamma)/\sigma = R\Delta\theta \cot(\gamma)/\sigma \tag{3.50}$$

Substituting for f_r from Eq.(3.49) gives

$$\Delta V_T = \frac{GR}{2\pi} \frac{\cot(\gamma)}{\sigma} \frac{\Delta\phi\Delta\theta}{r} \tag{3.51}$$

Substituting $r = R\sin(\theta)$ and taking the limit gives

$$V_T = \frac{G\cot(\gamma)}{2\pi\sigma} \int_0^{2\pi} \int_{\theta_1}^{\theta_2} \frac{d\theta}{\sin(\theta)} d\phi = \frac{G\cot(\gamma)}{\sigma} \left[\log(\tan(\theta/2)\right]_{\theta_1}^{\theta_2} \tag{3.52}$$

Similarly, the volume of compression members can be shown to be

$$V_C = \frac{G\tan(\gamma)}{\sigma} \left[\log(\tan(\theta/2)\right]_{\theta_1}^{\theta_2} \tag{3.53}$$

For loading *G* applied to equal circles at latitudes μ and $-\mu$ from the equator, substitution of $\theta_1 = \pi/2 - \mu$ and $\theta_2 = \pi/2 + \mu$ gives the loxodrome structure volume as

$$V_L = V_T + V_C = (G/\sigma) \log\left[\tan(\pi/4 + \mu/2)\right]\left[\cot(\gamma) + \tan(\gamma)\right] \tag{3.54}$$

where $\gamma = \cot^{-1}(FR/T)/2$. Equation (3.54) is pleasingly similar to Michell's original equation for the weight of a minimum-weight pure torsion loxodrome structure. For *F=0*, $\gamma = \pi/4$, parameter *G* is equal to torque *T* and Eq,(3.54) is then exactly the expression given in Michell's paper.

3.5. Comparison of Helical and Loxodrome Structures

Consider the loxodrome case: $\mu = \pi/3; \theta_1 = \pi/6; \theta_1 = 5\pi/6$. The corresponding helical structure has dimensions: *r=R/2*; $L = (2\sqrt{3})r$. The respective volumes for the condition *r*=1 are:

$$V_{cyl} = \frac{2\sqrt{3}G}{\sigma} \left[\frac{1}{\cos(\gamma)(1 + \tan^6(\gamma))^{1/2}} + \frac{1}{\sin(\gamma)(1 + \cot^6(\gamma))^{1/2}} \right] \tag{3.55}$$

where $\gamma = \cot^{-1}((Fr/T)/2)/2 = \cot^{-1}((FR/T)/4)/2$

$$V_{lox} = \frac{G}{\sigma} \left[\log(\tan(5\pi/12)(\cot(\gamma) + \tan(\gamma))\right] \tag{3.56}$$

where $\gamma = \cot^{-1}(FR/T)/2$

Figure 21 shows the comparison of Eqs.(3.55) and (3.56) plotted against angle η in Figure 12. The helical structure represents the global optimum solution for $\eta = 0$ since it has become in the limit a set of columns in pure compression. The loxodrome structure is the global optimum for $\eta = \pi/2$ which corresponds to pure torsion. This is the Michell solution with $\gamma = \pi/4$. The dashed curve represents the unknown globally optimal solution for combinations of axial and torsional loading, which are undoubtedly rotationally symmetric spiral structures, lying between the cylindrical and spherical envelopes.

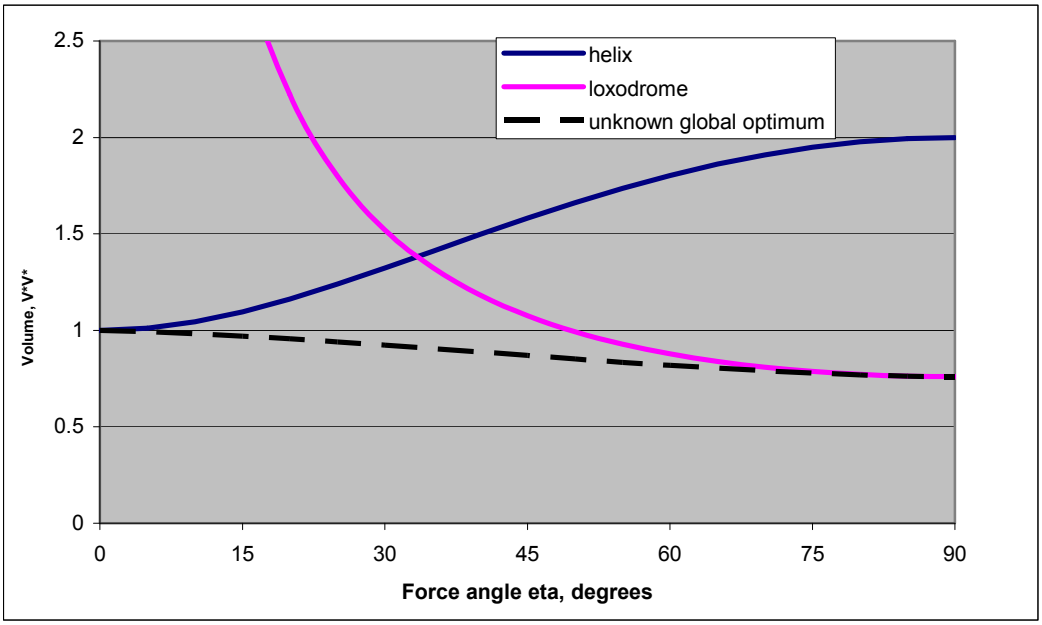

Figure 21. A Comparison of Helical and Loxodrome Structures.

3.6. Application of Topological Optimization

The minimum-weight structures defined above provide test cases for the validation of numerical topology optimization algorithms. One such algorithm is the finite element based adaptive topology optimization (ATO) procedure [18]. To demonstrate the performance of the ATO algorithm, several structural topologies were generated and compared with analytical solutions.

For the first set of solutions, the initial design domain considered is a tubular structure with the following dimensions

$$L = 15,\ R_i = 0.68,\ R_e = 1$$

where L is length of the structure, R_i is the interior radius, and R_e is the exterior radius. Note that the actual design domain is a solid cylinder of radius, R. Since the optimal topology consists of members located at the surface of the cylinder, for computational efficiency a thick walled cylinder is modeled. The wall thickness was selected to assure that the final topology does not reach the inner radius, R_i.

For convenience of specifying boundary conditions and generating the mesh, the structure was partitioned with three vertical cutting planes (the angle between planes is 120^o). The external boundary of one end of the tube is constrained such that it can move only in radial direction. As

shown in Figure 22b, the biaxial load (f_n along the longitudinal axis, f_t along the tangential axis) is applied on three points, at the external boundary of the other end of the structure.

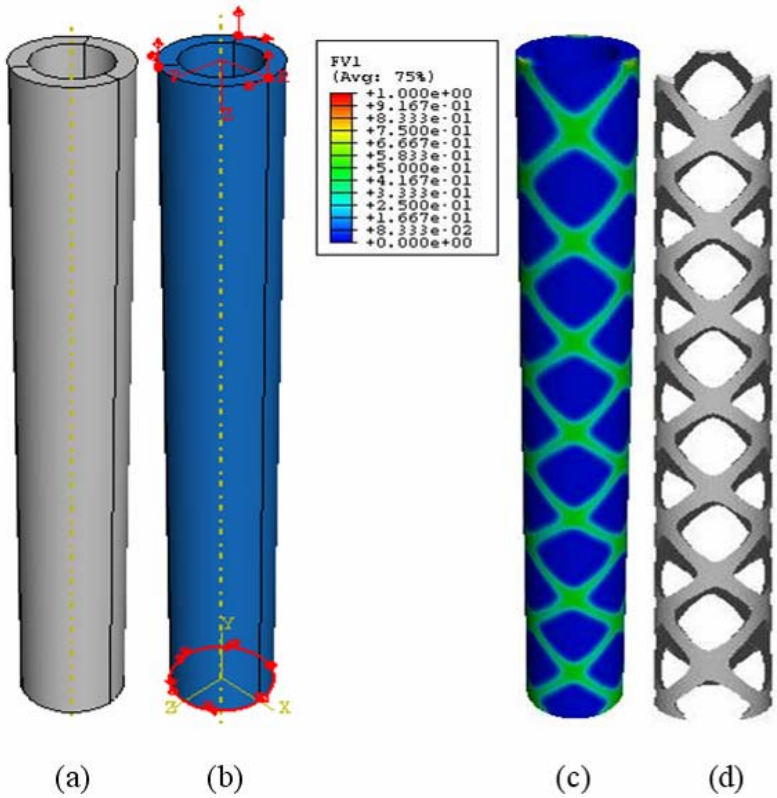

Figure 22. Tubular Structure Design Domain (a), Boundary Conditions and Applied Load (b), Final ATO Density Distribution (c), and Predicted Topology (d).

The domain was discretized using 8 node hexahedral elements. For the cases discussed below, the optimal topologies were identified in less than 100 finite element iterations. For the case of f_n=0 (pure torsion), the optimal topology is helical spirals oriented ±45° to the axial direction. The load and boundary conditions, final density distribution and STL CAD model for this case are shown in Figure 22(b and c). The STL models are created by custom software that applies the marching cube algorithm [19] to identify triangulated surfaces that correspond to the interface between fully dense regions and regions of essentially zero density,
To examine the effect of combined axial and torsion loads, eight different ratios f_n/f_t were analyzed using the ATO algorithm. The results are presented in Figure 23. For these structures, the angle between the tension members and the axial direction is estimated using

$$\gamma_{ATO} = \tan^{-1}\left(\frac{R_e\theta_T}{L}\right) \tag{3.57}$$

where θ_T is the angle of rotation of the tension members about the longitudinal axis. The estimated helix angles are compared to the theoretical values in Table 1. This comparison is shown graphically in Figure 24. The estimated angles for the tension members obtained with the ATO algorithm are shown to correlate very well with the analytical results.

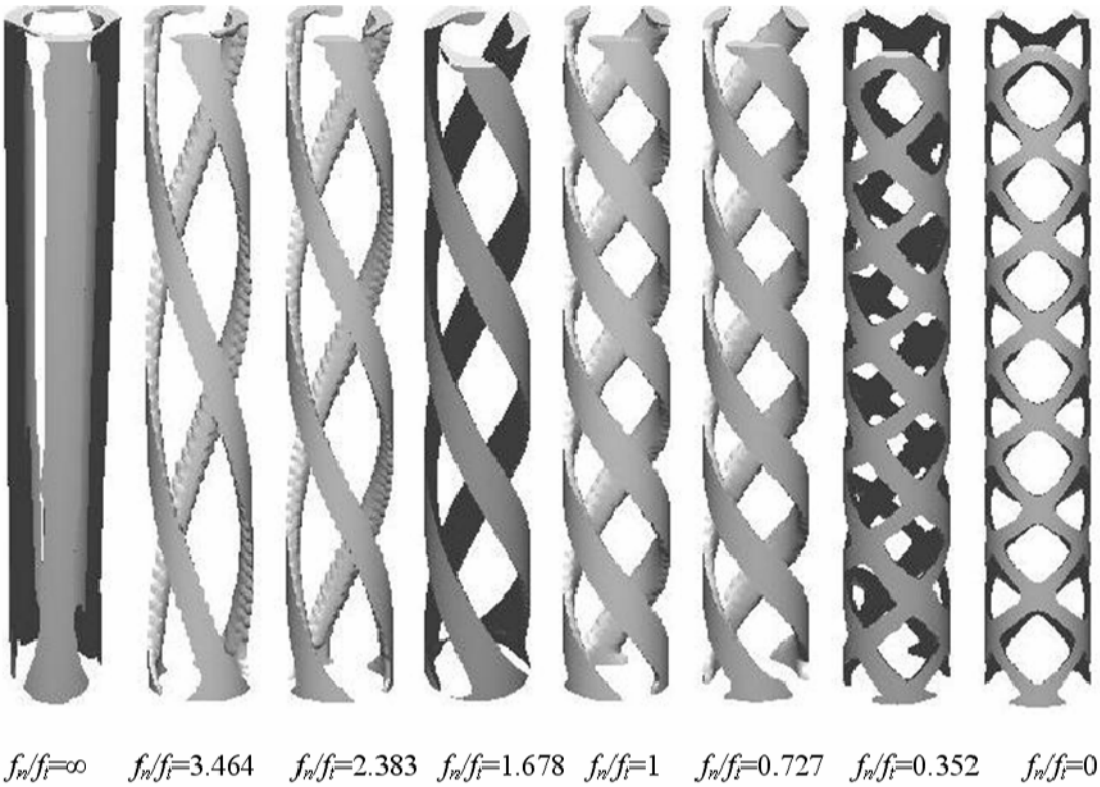

Figure 23. ATO Predicted Topologies for Combined Loading from Fully Normal (left) to Fully Torsional (right).

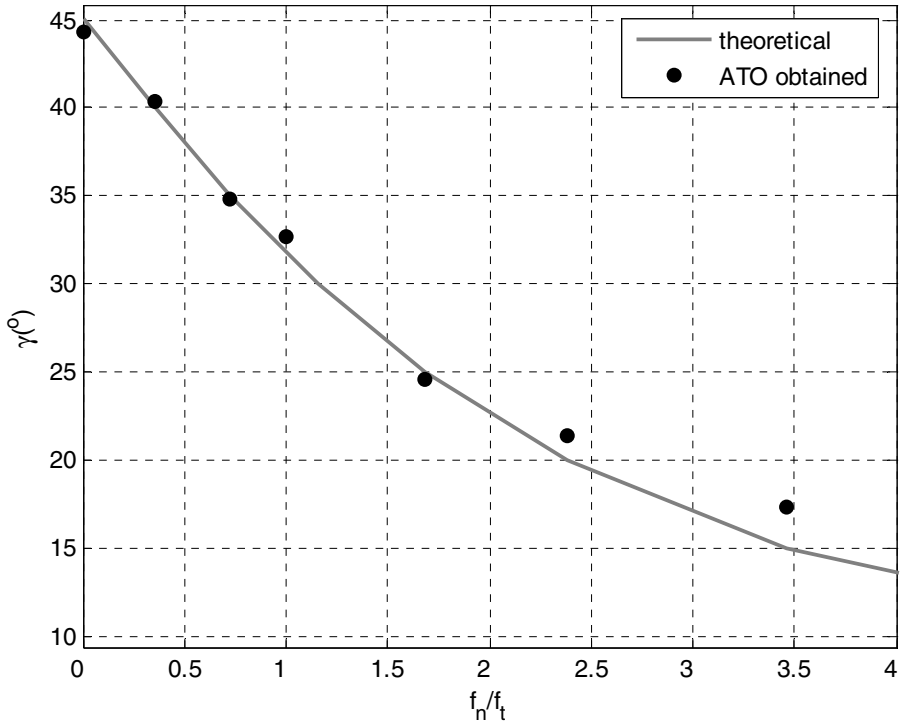

Figure 24. Theoretical Optimal Orientation Versus ATO Predicted Orientation for the Tension Member and Different Ratios f_n/f_t.

Table 1 . Comparison of ATO Results and the Analytical Predictions.

f_n/f_t	V	*Number of elements*	θ_{ATO}	γ_{ATO}	γ_{th}
0	0.05	49632	4.66π	44.34^o	45^o
0.352	0.05	49632	4.06π	40.39^o	40^o
0.727	0.05	49632	3.32π	34.83^o	35^o
1	0.05	19584	3.06π	32.65^o	31.7^o
1.678	0.05	19584	2.18π	24.58^o	25^o
2.383	0.05	49632	1.87π	21.43^o	20^o
3.464	0.05	49632	1.49π	17.33^o	15^o
∞	0.05	49632	0π	0^o	0^o

As the ratio of axial to torsion load increases, the relative size of the tension members to that of the compression members increases. Similarly, as the f_n/f_t ratio increases, the load carried by the compression members diminishes. Examination of the topologies shown in Figure 23 reveals that for angles $\gamma < 40^0$, the compression members become too small to be included in the final topologies. In an attempt to reveal the presence of these compression members, a series of cases were analyzed in which the design volume was increased and the element size was reduced. For the case $f_n/f_t=1$, the design volume was increased to 0.12. Figure 25 shows the results for three different mesh densities. Note that for the two finer meshes (19584 and 49632 elements), small compression members normal to the tension members are predicted as expected. As the design volume is increased further, the optimal topology converges to a solid wall tube (see Figure 26).

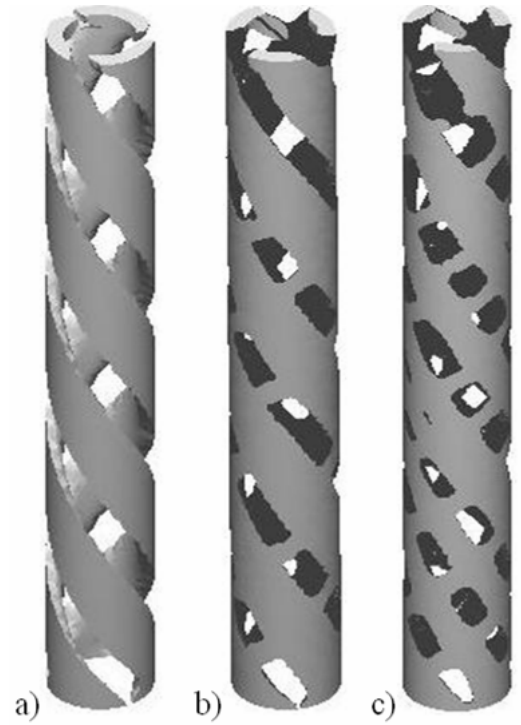

Figure 25. Results for f_n/f_t=1, v_f=0.12 and: a) 5452 Finite Elements, b) 19584 Finite Elements, and c) 49632 Finite Elements.

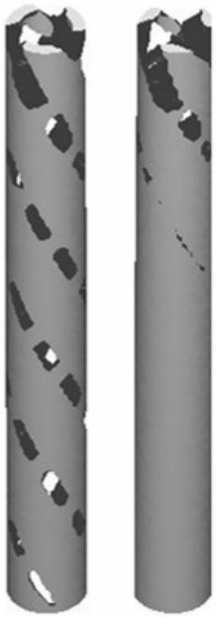

v_f=0.15 v_f=0.25

Figure 26. Results for f_n/f_t=1.

The second test case also involves torsion loading. In this case, the ATO analysis considered an infinite design domain that was approximated by a thick wall cylinder (Figure 27) in which the

circumferential forces were applied along a circular path near the inner diameter of the cylinder. At the opposite end of the cylinder, nodes along the corresponding circular path are constrained such that motion in the axial and circumferential directions is prevented. The STL model created using the ATO results reveals a loxodrome structure (Figure 28 left). This topology matches that predicted by Michell in 1904. A physical model (Figure 28 right) was fabricated on the Dimension SST 3-D printer with no difficulty.

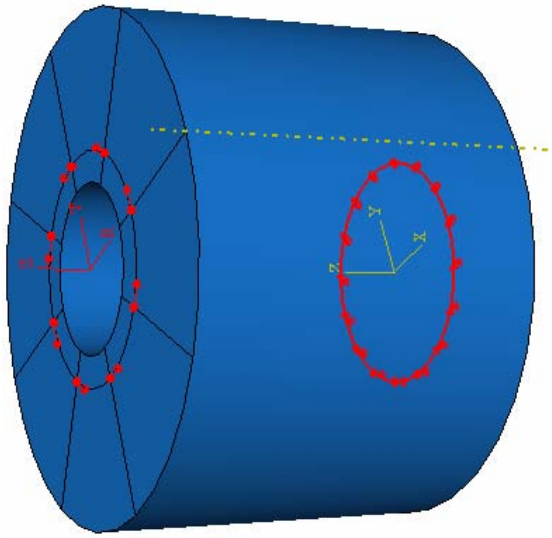

Figure 27. Test Case 2 - Design Domain and Boundary Conditions.

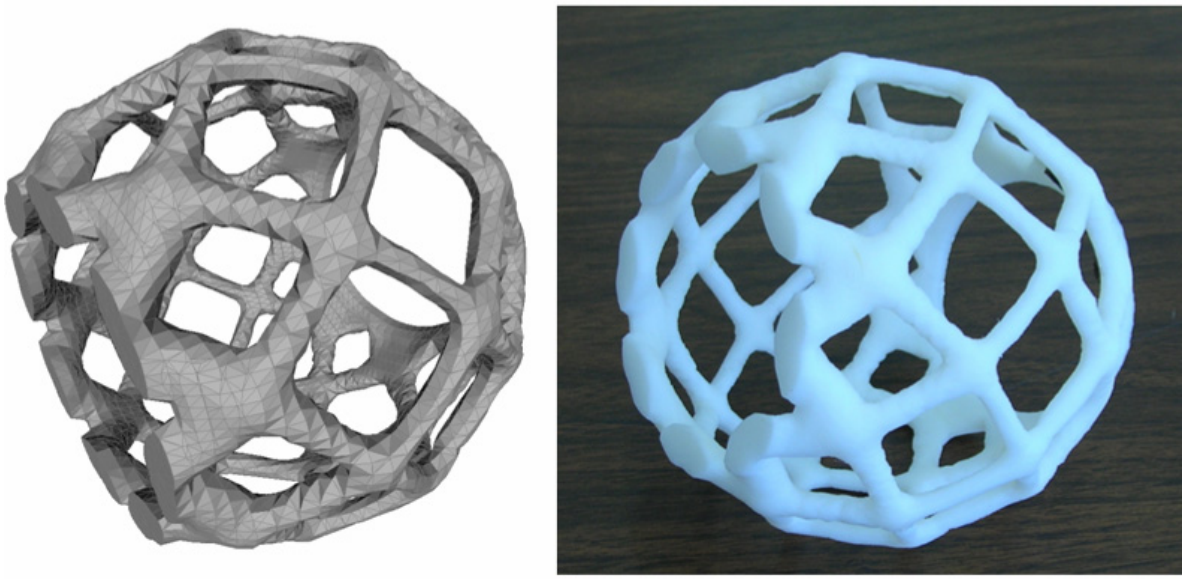

Figure 28. Test Case 2 STL Model (left) and Rapid Manufactured Part (right).

3.7. Discussion

Generalized minimum-weight structural layouts, for the support of any combination of axial and torsional loading, have been developed. These have been based on families of cylindrical helices

and families of spherical loxodromes. The work has laid the foundation for further studies of globally optimal structures for the transmission of axial and torsional loading.
The principal intention in this work is to provide test cases for numerical topological optimization. It is anticipated that the solutions may present a challenge, since for the small angular spacing of the truss elements the internal radial force component is always of the order of magnitude of the angular spacing for any arbitrary selected pair of helix or loxodrome families. However, for a true pin-jointed truss structure this would certainly give rise to significant radial displacements leading to failure.

The analyses presented in this report can readily be carried out without using the small angle approximation for the trigonometric functions. However, this leads to an analytically intractable set of equations, which must be solved numerically. Also the results depart further from the Michell solutions which are the target for 3-dimensional numerical topological optimization studies.

As mentioned in the introduction, the helical solutions presented here can only be considered optimal with respect to other structures which lie on a cylindrical envelope. If the loading system is pure torsion then the global optimal structure follows rhumb lines or loxodromes over a spherical surface. Michell argued this point through the possibility of extending the loxodrome strain field radially outwards. A simple analytical proof of global optimality has been established by the authors.

For pure axial loading the set of straight parallel columns equi-spaced on a pitch circle is the globally optimal solution. For this uniaxial case any structure, outside of the cylindrical envelope, must carry internal forces whose axial components equal the axial loading. The members will thus be longer and carry larger internal forces; both contributing to additional weight. The globally optimal family of structures, to support combined axial and torsional loading, is therefore expected to range between the spherical loxodrome solution for pure torsion and the parallel-columns solution for pure axial load. This is represented by the dashed curve in Figure 21.

These minimum-weight layouts are used to demonstrate that the finite element based ATO scheme is an effective tool for the identification of minimum weight topologies. Several 3-D cases are presented for structures subjected to combined tension-torsion loading. The algorithm has been implemented through the use of user subroutines used in conjunction with the commercial finite element analysis package, Abaqus. The use of Abaqus' graphical user interface and pre-processing capabilities simplifies the determination of optimal topologies for general design problems. In addition, software has been developed to extract 3-D surfaces from the ATO results by defining triangulated surfaces that describe the optimal topology. This surface definition is saved in standard STL file format. The STL files may be used in conjunction with rapid manufacturing equipment for the manufacture of minimum weight structures. Taken together, these software tools provide a powerful tool for use in the design of minimum weight structures.

4. MULTI-ARCH 3-DIMENSIONAL MICHELL STRUCTURES: CASE STUDIES FOR NUMERICAL TOPOLOGICAL OPTIMIZATION

The loxodrome structures that were developed through analytical optimization did a lot to verify the solutions achieved by 3D ATO. The team continued to investigate other optimized solutions using multi-arch structures. This chapter is a paper with the same title as the chapter title that will be submitted to the *Joint 8th World Congress on Computation Mechanics (WCCM8) and the 5th European Congress on Computational Methods in Applied Sciences and Engineering (ECCOMAS 2008)* with the authors being Peter Dewhurst and David Taggart.

4.1. Abstract for Paper

A family of 3-dimensional tripod structures is established from a generalization of the Michell 90-degree arch beam structure. It is shown that tripod structures of reduced height can be obtained by introducing additional arches along great circle segments of a hemispherical shell envelope, thus forming a spherical triangle of secondary Michell arches. Reduced height structures formed in this way provide locally optimal solutions which converge very rapidly to the known globally optimal Michell solution as latitude angle increases. The analytical structures established in this paper are intended to provide challenging test cases for numerical structural optimization procedures.

The tripod structures can be generalized to ones with any number of supports around a pitch circle, and a load applied at the circle center. In these cases, structures of reduced height can be obtained by providing a set of Michell arches connecting a spherical polygon.
The application to these problems of a novel numerical topological optimization procedure is described.

Nomenclature

β	angle subtended by side of spherical triangle
δ	vertical deflection of structure
$\varepsilon_T, \varepsilon_C$	constant stain magnitudes in structural members
ϕ	angle of latitude
θ	angel of longitude
σ_T, σ_C	stress magnitude in tension and compression structural members
ω	rotation of structural members during deformation
A	cross-sectional area of structural member
a, r	radii of circular arcs
f	force magnitude on structural member
F	external load on structure
l	length of structural member
V	volume of structure

4.2. Introduction for Paper

Michell [1] laid down the requirements for optimum structural frameworks over 100 years ago. Among other layout examples, his paper included a simply supported semi-circular arch beam and a minimum-weight torsion structure. The latter structure is based on a spherical strain field, which is compatible with pure torsion about the spherical axis, and in which the maximum and

minimum strains have the same constant magnitudes and follow the two families of opposite 45-degree loxodromes.

It will be shown in this paper that a different family of 3-dimensional minimum-weight structures can be obtained from the combination of Michell arches on a hemispherical envelope. In these structures great circles are subjected to constant strain magnitude in compression, and all of the radial directions are subjected to constant strain magnitude in tension.

Such structures can comprise a set of 90-degree Michell arches, starting from support points around a pitch circle, and meeting at the pole. However, a set of very-near optimal solutions can be formed by joining the primary arches along great circle directions, before reaching the pole. This is explored in the paper for the simplest case of three equi-spaced arches, joined by a spherical triangle of secondary Michell arch structures. The existence of these very-near optimal structures provides a challenge for numerical topological optimization procedures. This will be explored in the paper. In particular, the recently developed finite element based adaptive topology optimization (ATO) algorithm developed by Taggart and Dewhurst [18] is investigated

Before proceeding to develop the spherical structures it is worthwhile first to review some of the properties of the Michell arch structure. This will be carried out in the next section.

4.3. Michell's Semi-Circular Arch Beam

The simplest possible Michell beam, based on the so-called centered-fan construction is shown in Figure 29(a). Figure 29(b) shows the corresponding force diagram. The analysis below is taken from Srithongchai et al.[20].

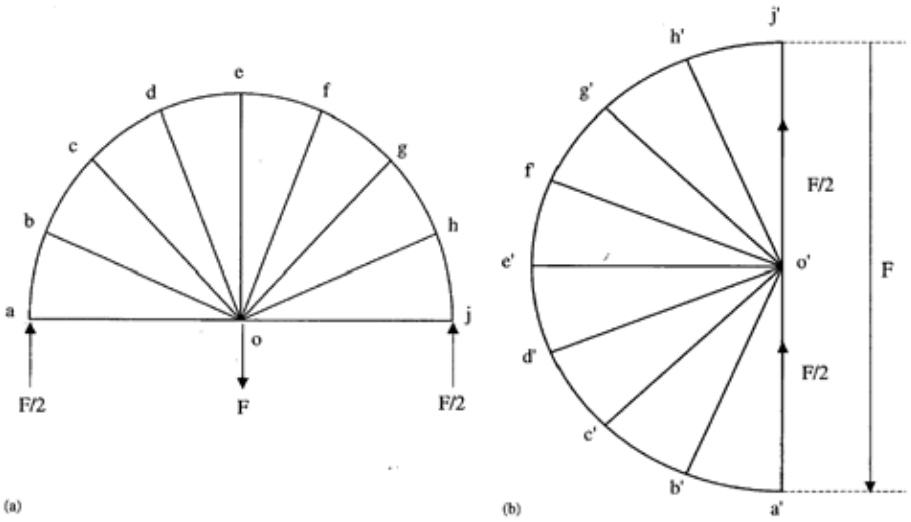

Figure 29. Layout of Michell Circular Arch Beam(a) and Corresponding Force Diagram(b).

It is worth noting that this was also developed as an optimum disk of varying thickness by Kozlowski and Mroz [21]. The design contains a single circular arc outer flange, which carries the concentrated support loads. The mathematical model comprises an infinite number of infinitesimally thin radial members, which carry the tensile force distribution from the

application of the center load, F. Under the action of this force distribution the tension members will increase in length, and the circular arc will decrease in length under the action of the support forces. Assume that the flange has maximum allowable compressive stress σ_C, and the spokes have maximum allowable tensile stress σ_T. Following the approach established by Hemp [4], the volume of the structure can be determined by subjecting the flange to a virtual compressive strain $\varepsilon_C=\varepsilon\sigma/\sigma_C$ and the spokes are subjected to virtual tensile strain $\varepsilon_T=\varepsilon\sigma/\sigma_T$. The effect is shown exaggerated in Figure 30. Note that from the deformed circular arc geometry, the angle of the centered-fan structure has decreased to satisfy

$$\phi = \pi \frac{(1-\varepsilon_C)}{(1+\varepsilon_T)} \tag{4.1}$$

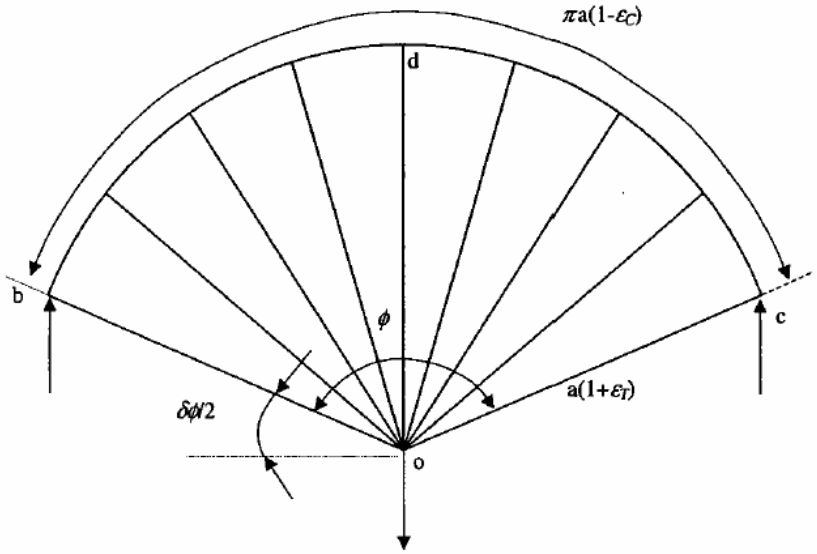

Figure 30. Deformation Mode of Centered Fan.

However, angular changes in Michell structure members are defined by

$$\omega - (\varepsilon_T + \varepsilon_C)\phi \;=\; \text{constant along an } \alpha\text{-line} \tag{4.2a}$$

$$\omega + (\varepsilon_T + \varepsilon_C)\phi \;=\; \text{constant along an } \beta\text{-line} \tag{4.2b}$$

where ϕ is the angle turned through from the base point of a structural member and ω is the angle of rotation with respect to the base point. These equations were presented by Hemp [12] and are a generalization of Hencky's equations relating pressure to yield shear stress in slip-line field theory.

Referring to Figure 30, the rotation of α-member od is zero by symmetry. Thus using Eqs. (4.2) the rotation of α-members oc and ob are

$$\omega_{oc} = (\varepsilon_T + \varepsilon_C)(\pi/2) \tag{4.3}$$

and $$\omega_{ob} = -\omega_{oc}$$

Thus the angle of the centered-fan after deformation is

$$\phi = \pi - (\varepsilon_T + \varepsilon_C)\pi \tag{4.4}$$

which is equivalent to Eq. (4.1) for small elastic strains.

In the space diagram of the structure shown in Figure 29(a), radial members *oa*, *ob*, etc. are representatives of an infinite array of radial tension members. The prime superfix is then used to denote corresponding locations on the force diagram in Figure 29 (b). Arc $b'c'$ in the force diagram, for example, represents the force distribution carried by the radial tensile members meeting the outer arc between *b* and *c*. In general the force diagram, defined in this way is composed of curves which are everywhere normal to the curves of the structure itself. Such force diagrams therefore satisfy the equiangular property of the Michell structures and will be defined by the same set of differential equations [12].

The volume of a structure can be represented as

$$V = \sum lA = \frac{1}{\sigma_T}\sum_T lf + \frac{1}{\sigma_C}\sum_C lf \tag{4.5}$$

where *l* is the length, *A* the cross-sectional area of a structural element, σ_T, σ_C the maximum allowable stress values in both tension and compression respectively, and the summations include all tensile and compression structure elements. For the virtual strain field defined in Hemp's approach, where $\sigma_T\varepsilon_T = \sigma_C\varepsilon_C = \sigma\varepsilon$, (5) can be transformed to the virtual energy relationship

$$V\sigma\varepsilon = \sum_T f(l\varepsilon_T) + \sum_C f(l\varepsilon_C) = \sum F_i u_i \tag{4.6}$$

where *f* are the forces carried by the structural members, F_i are the externally supported loads and u_i are the corresponding virtual displacements of the external loads. Hence the volume of a Michell structure can be given by [21]

$$V = \frac{1}{\varepsilon\sigma}\sum_{i=1}^{n} F_i u_i \tag{4.7}$$

and knowledge of the relative contribution to $\sum fl$ from tension and compression members is not needed. In Michell's original paper this problem did not arise since his examples could be shown to contain equal amounts of $\sum fl$ from tension and compression members.

For the deformed beam shown in Figure 30 the displacement of the load is,

$$u = a(1 + \varepsilon_T)\,\omega_{oc} = \pi(\varepsilon_T + \varepsilon_C)a/2 \tag{4.8}$$

and substituting into (4.7) with span $L = 2a$ gives

$$V_\pi = \frac{\pi Fa}{2}\left(\frac{1}{\sigma_T} + \frac{1}{\sigma_C}\right) \tag{4.9}$$

Alternatively, this result can be obtained directly from Eq.(4.5). In order to present this in more general terms, which can be used to estimate the volume of the spherical-layout structures, we will define the volume of an arbitrary sub-span, angle θ, of the arch beam in terms of the flange force transmitted from the supports. In the present case the compressive force in the flange is simply $F_{flange} = F/2$. Multiplying the circular flange length by F_{flange} gives the flange volume as $F_{flange}a\theta/\sigma_C$. The volume of the radial members can be obtained by integrating the product of radius (spoke length) and the incremental radial cross-sectional area $F_{flange}\delta\theta/\sigma_T$, over the range *0* to θ, which gives $F_{flange}a\theta/\sigma_T$. The total volume a span through angle θ of a Michell arch structure can thus be represented by

$$V_\theta = F_{flange} a\theta \left(\frac{1}{\sigma_C} + \frac{1}{\sigma_T}\right) \tag{4.10}$$

The volume calculated in this way, is of a theoretical structure which contains a continuous distribution of structural elements. For application it is necessary to replace this continuous distribution by a set of discrete members, each of which will carry a concentrated force equivalent to the force distribution over a given angular range. For example, the line diagram in Figure 29(a) represents such a discrete approximation with 22.5 degree spacing between members. The compression members along the arc *ab*, *bc*, cd, etc., would in this case be approximated by the straight chord segments. Analysis of this truss, using the method of joints, can readily verify its volume to be

$$V = 1.5913 Fa \left(\frac{1}{\sigma_C} + \frac{1}{\sigma_T}\right) \tag{4.11}$$

This volume is only 1.3 percent larger than the theoretical continuum model; see Demircubuk [22].

4.4. Spherical Beam Structures

We define a hemispherical strain field with an infinite number of equally distributed radial members meeting at the center. The radial members are subjected to tensile strain ε_T, so that under the action of a vertical center load, the radial members increase in length by factor $(1+\varepsilon_T)$. The shell is supported at the equator in such a way as to allow unconstrained expansion of and rotation about its circumference during loading. All of the 90-degree great circle arches forming the lines of longitude are subjected the compressive strain ε_C. This field will be referred to the Michell hemisphere, since every two-dimensional section along a longitude line forms a Michell arch with properties discussed in section 4.3.

4.4.1. Tripod Structures

The simplest truly 3-dimensional structures based on great circle arc layouts on the Michell hemisphere are those with three support points on the equator, and a vertical load applied at the center. For further simplicity the supports will be equi-spaced. If the allowable structure height can be equal to or greater than the pitch circle radius of the supports, then it is clear that a structure comprising three 90 degree centered fans is a globally optimal analog of the Michell 2-dimensional arch. This structure is illustrated in Figure 31.

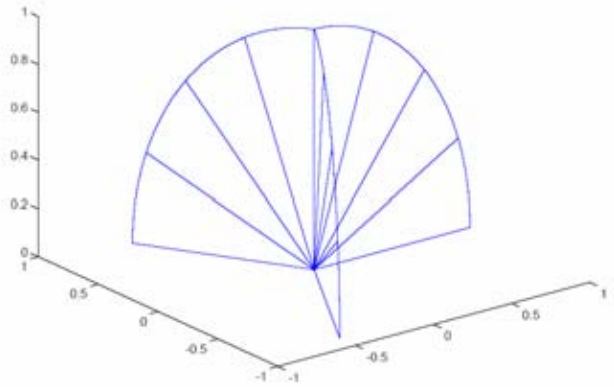

Figure 31. Tripod Michell Arch Structure.

It is clear that the minimum volume of this structure is identical to that of the Michell arch; the reaction forces carried by the arch flanges have magnitude *F*/3 and equivalence follows from applying Eq.(4.10) to the three 90 degree arches. However, while there is no possible simple modification for the 2-dimensional Michell arch for reduced height, a simple height reduction modification does exist for the tripod arch structure. At any latitude, as the structure builds upwards from the support and load points, it is permissible to join the growing circular arches with three additional great circle arches to form a spherical triangle. The added circular arches, which form a crown to the structure, must then be supported by additional radial members reaching down to the loading point. Note that, in this case, the rotation of the horizontal radial members (denoted $\delta\phi/2$ in Figure 30) will now be greater to provide compatibility of displacements with the contracted length of the three upper arches.

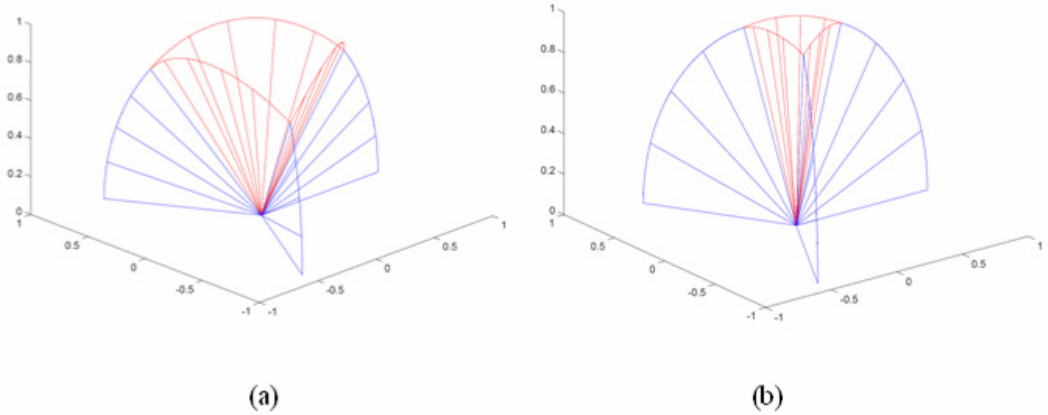

(a) (b)

Figure 32. Reduced Height Tripod Arch Structures Rising to 45˚(a) and 75˚(b) Latitude.

Two examples of this family of structures are illustrated in Figure 32. In the Figure 32(a) the primary outer arches rise to 45˚ latitude and Figure 32(b) shows the spherical triangle starting at 75˚ latitude. The two sets of arches are shown in different color to indicate that they are separate analytic regions, which together define a kinematically permissible displacement field. This makes the solutions only locally optimal with respect to a domain extending upwards to the level on the spherical triangle. If we allow a domain higher than the full hemisphere, then following Hemp's proof of optimality [12] the Michell hemisphere can be used as the test virtual strain field. Subjected to this strain field, the spherical triangle arches are subjected to strain values ε which lie between the minimum and maximum values; i.e. $\varepsilon_C < \varepsilon < \varepsilon_T$. Thus Hemp's proof establishes that the volume of the full arch structure (Figure 31) will always be less than the volume of the reduced height structures shown in Figure 32. The difference between these volumes can readily be determined with access to some results from spherical trigonometry.

For the case of the spherical triangle vertices on the same latitude angle, θ, separated by 120˚ of longitude, the general expression for the angle subtended by an arc of great circle triangle sides reduces to

$$\beta = \cos^{-1}[\sin^2(\theta) + \cos^2(\theta)\cos(2\pi/3)) \tag{4.12}$$

for the triangle sides.

An elegant expression established by Mungon [23] for the interior angle of a spherical equilateral triangle is

$$\alpha = \cos^{-1}(\tan(\beta/2)/\tan(\beta)) \tag{4.13}$$

From Eq.(4.10) the volume of the three lower centered fans is

$$V_{lower} = Fa\theta(\frac{1}{\sigma_C} + \frac{1}{\sigma_T}) \tag{4.14}$$

From equilibrium, the compressive flange force in the upper arches is

$$F_{flange} = F/6\cos(\alpha/2) \tag{4.15}$$

and so application of Eq.(4.10) gives the volume of the three upper centered fans as

$$V_{upper} = \frac{Fa\beta}{\cos(\alpha/2)}(\frac{1}{\sigma_C} + \frac{1}{\sigma_T}) \tag{4.16}$$

A dimensionless volume parameter which compares the reduced height tripod structure to the Michell arch is thus

$$V^* = V_\pi/(V_{lower} + V_{upper}) \tag{4.17}$$

This parameter will of course be greater than 1.0 since V_π is globally optimal, and it will converge to 1.0 as θ approaches $\pi/2$. A plot of V^* against latitude is given in Figure 33.

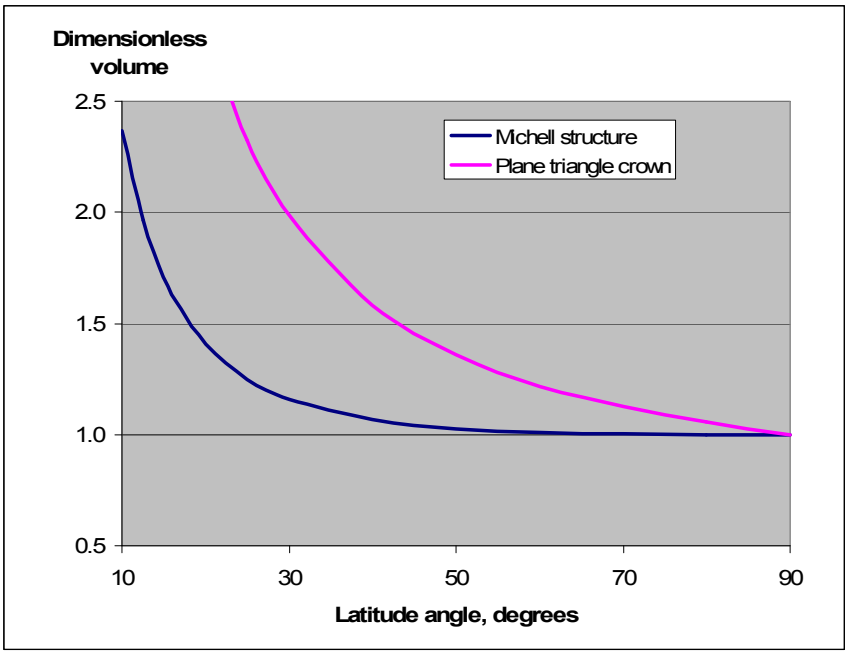

Figure 33. Dimensionless VColume Plots of 6-Arch Michell Structure and Approximation with Plane Triangle Crown.

It can be seen that the volume of the structure converges extremely rapidly to the absolute minimum volume when the latitude angle of the structure increases beyond 45 degrees. To appreciate the surprising efficiency of this structure it is instructive to approximate the three inner arches with a plane equilateral triangle across the crown. This approximation is illustrated in Figure 34. The volume of the six-bar pyramid truss system is obtained as follows. The lengths of the crown triangle sides are

$$l_{crown} = 2a\sin(\beta/2) \tag{4.18}$$

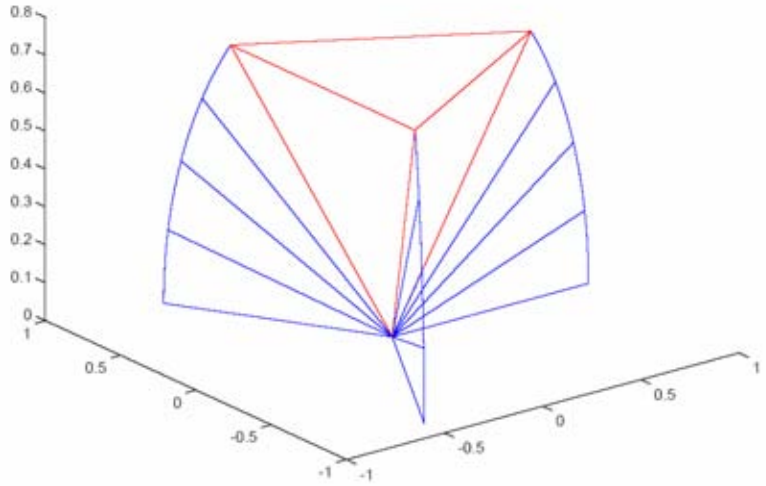

Figure 34. 6-Arch Michell Structure Truncated with Equilateral Triangle Truss Crown.

and the force in the crown triangle members is

$$F_{crown} = F/(\sqrt{3}\sin(\theta)) \tag{4.19}$$

The sides of the pyramid structure are of radial length, a, and carry force

$$F_{sides} = F\cot(\theta) \tag{4.20}$$

The volume of the pyramid structure is thus given by

$$V_{pyramid} = F_{crown} l_{crown}/\sigma_C + F_{sides} a/\sigma_T \tag{4.21}$$

The quantities $F_{crown} l_{crown}$ and $F_{sides} a$ are, in fact, numerically identical although the establishment of this equality from the trigonometric relations has proved to be elusive. Replacing V_{upper} in Eq.(4.17) with $V_{pyramid}$ gives the upper curve in Figure 32. This shows that the structure is substantially heavier than the Michell structure except for latitude angles approaching the pole.

4.5. Advanced Topological Optimization

The adaptive topology optimization (ATO) algorithm required that the design domain, loads and boundary conditions be represented by a finite element model. For Michell arch structures, the design domain is semi-infinite. This domain is approximated as a cylinder with a radius 10% larger and a height 50% higher than the support circle radius, taken to be unity. Symmetry conditions are imposed such that only a sector of this cylinder needs to be modeled. As shown in Figure 35 for the case of three supports (n=3), a sector swept through a 60° provides an appropriate model. Other cases considered, n=2, 4, 5, and 6, required sector angles of 90°, 45°, 36° and 30°, respectively. A concentrated force in the axial direction is applied at the origin. The supports were modeled by constraining the axial displacement of one point located at (r,θ,z)=(1,0,0). Symmetry conditions are imposed by constraining faces with θ=0° and 60° (for n=3) such that the circumferential displacement, u_θ, is zero. Finally, nodes along the edge r=0 are constrained to have zero radial displacement.

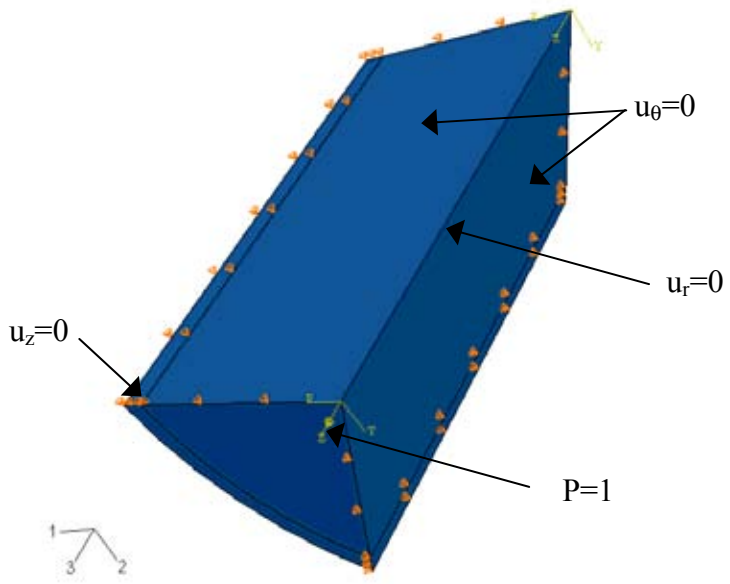

Figure 35. Tripod Structure Test Case 1 - Design Domain (n=3).

Post-processing of the ATO results include the generation of STL CAD files using an implementation of the marching cube algorithm [19] to define triangulated surfaces corresponding to the surface of the fully dense regions. This STL generation code includes the capability to impose mirroring such that the full structure is generated.

The resulting topology for the tripod (n=3) test case is shown in Figure 36. Using a coarse mesh and relatively few ATO iterations (Figure 36a), the expected topology of three Michell arches is apparent. Refining the mesh and increasing number of iterations (Figure 36b and Figure 36c) results in the near-optimal truncated arch structure discussed above. Initially, it was believed that this truncated structure was due to a domain height that was insufficient. Increasing the domain height was found to have little effect on the results. The final topology is sensitive to mesh density, number of iterations and design volume, v_f, as shown in Figure 36(a –d). Examination of these results reveal that as the Michell arches develop, radial members emerge from the load point to the outer flanges. Theoretically, Michell arches contain an infinite number of members of infinitesimal size. In the numerical results, the number of members and the member size is sensitive to the mesh density, number of iterations and design volume. If, for a given case, no radial member grows vertically toward the apex of the arch, flange members exhibit a tendency to join with adjacent flanges before reaching the apex. This effect is most pronounced in cases with an odd number of supports where flange members are not able to merge with opposing co-planar flanges.

The predicted optimal topology for cases where n=2, 4, 5 and 6 are shown in Figure 37. In all of these cases, the expected topology of n Michell arches that meet at the apex is observed. These test cases demonstrate that the ATO method successfully identifies the optimal, or for the case n=3, near-optimal topology.

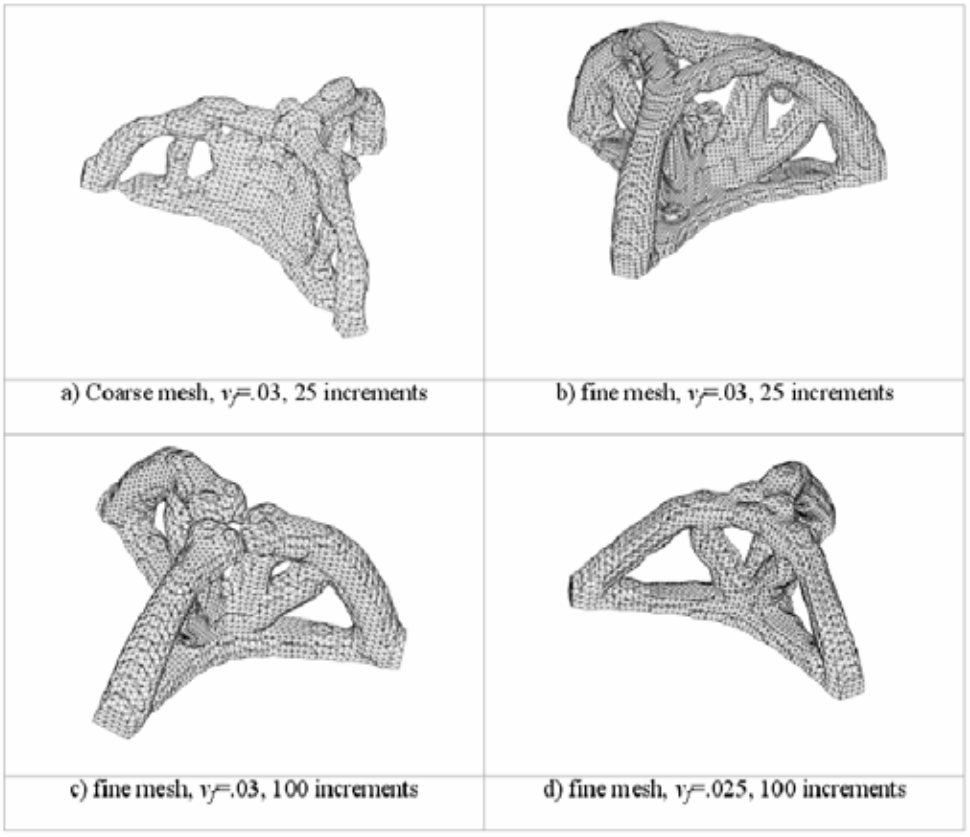

Figure 36. ATO Results for Arch Test Case 1, n=3.

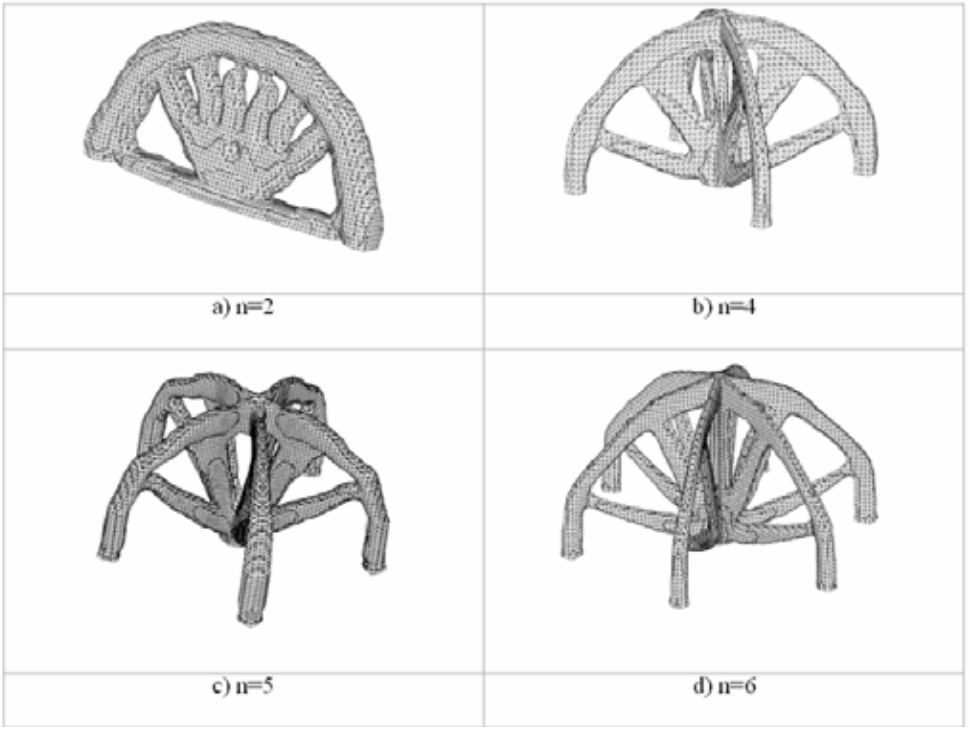

Figure 37. ATO Results for Case1 with n Legs where n=2, 4, 5, 6.

4.6. Conclusions

A globally optimal tripod support structure can be formed from three 90-degree Michell arches. If the height of the structure is limited below that of the hemispherical pole, then a locally optimal solution can obtained by replacing the top portion of the 90-degree arches with a spherical equilateral triangle and supporting radial members. The resulting 6-arch structure converges extremely rapidly to the globally optimal solution as the latitude angle of the primary arches is increased.

A simple approximation to the secondary arches and supporting radial members can be obtained by substituting an inverted pyramid truss with equilateral upturned base. This is a far less efficient structure, mainly due to the increased force magnitudes resulting from slope discontinuity between the primary arches and the flat triangle truss crown.

The purpose of this work is to provide a 3-dimensional case for testing the efficiency of numerical structural optimization procedures. These procedures will usually assign or transfer material density to regions of highest strain energy. This tends to produce structural 'growth' outwards from load and support points. For the proposed test case two measures of the ability of the numerical procedures are intended:

- How symmetrical is the numerically obtained structure?
- How far towards the pole has the structure extended, before terminating with an equilateral triangle?

5. FLEXFEM DEVELOPMENT

This section provides a summary of code development for topological optimization algorithms at Sandia within the context of this project. This method utilizes the eXtended Finite Element Method (X-FEM) code as the FEM backbone for this optimization code.

5.1. Model Equations

The objective is to find the part geometry that minimizes compliance, C, under a given set of constraints and loads:

$$\min_{\phi} C(\phi) \tag{5.1}$$

where

$$C = \int_{\gamma_t} \mathbf{u}^T \mathbf{t} d\Gamma \tag{5.2}$$

and the function, $\phi(\mathbf{x})$, implicitly defines the part geometry:

$$\begin{array}{ll} \phi(\mathbf{x}) = v & on\ \Gamma \\ \phi(\mathbf{x}) > v & inside\ \Omega \\ \phi(\mathbf{x}) < v & outside\ \Omega \\ \phi(\mathbf{x}) = \alpha & for\ \phi(\mathbf{x}) > \alpha \\ \phi(\mathbf{x}) = -(\alpha - \gamma) & for\ \phi(\mathbf{x}) < -(\alpha - \gamma) \end{array} \tag{5.3}$$

The displacement, **u**, must satisfy conditions of static equilibrium, $\nabla \sigma = t$, and the geometry is constrained to yield the desired material volume.

5.2. Discrete Form

Following the notation in [25], the equilibrium displacements are found by

$$\int_{\Omega_{des}} \bar{H}_1(\phi(\mathbf{x}))\, \mathbf{B}_I^T \sigma\, d\Omega = \int_{\Gamma_t} N_I \mathbf{t}\, d\Gamma \tag{5.4}$$

where $\mathbf{B}_I$ is the symmetric gradient matrix and N_I are the nodal basis functions. The discrete representation of the geometry is

$$\phi(\mathbf{x}) = \sum N_I \phi_I \tag{5.5}$$

in terms of the nodal values. The geometry is updated iteratively according to

$$\begin{aligned} \phi_I^{new} &= (\phi_I + \alpha) A_I^{\eta} - \alpha \\ A_I &= \frac{\int_{\Omega_{des}} \bar{H}_1'(\phi(\mathbf{x}))\, N_I \epsilon^T \mathbf{C} \epsilon\, d\Omega}{\lambda_2 \int_{\Gamma_{des}} \bar{H}_2' N_I\, d\Omega} \end{aligned} \tag{5.6}$$

The constant, η serves to dampen ϕ_I. The functions $\overline{H}_1$ and $\overline{H}_2$ in the preceding are given as

$$\bar{H}_1(\phi) = \begin{cases} \Delta & \phi \le -(\alpha-\gamma) \\ \frac{1}{4}\left(1+\sin\frac{\pi\phi}{2l}\right)^2 & -(\alpha-\gamma) < \phi < \alpha \\ 1 & \phi \ge \alpha \end{cases}$$
$$\bar{H}_2(\phi) = \begin{cases} \Delta & \phi \le -(\alpha-\gamma) \\ \frac{1}{2}\left(1+\sin\frac{\pi\phi}{2l}\right) & -(\alpha-\gamma) < \phi < \alpha \\ 1 & \phi \ge \alpha \end{cases} \tag{5.7}$$

The constant, λ_2, is found by recursive bisection such that the volume constraint

$$\int_{\Omega_{des}} H(\phi(\mathbf{x}))d\Omega = V_o \tag{5.8}$$

is satisfied.

To avoid numerical instabilities that can arise such as checker-boarding and mesh dependence [26] the nodal sensitivities, A_I, are filtered at each iteration. The filter takes the form

$$\hat{A}_I = \frac{1}{\sum_{J=1}^{N}\hat{F}_{IJ}\phi_J}\sum_{J=1}^{N}\hat{F}_{IJ}\phi_J A_J. \tag{5.9}$$

where $\hat{F}_{IJ}$ is a weight factor,

$$\hat{F}_{IJ} = \frac{3}{\pi R^2}\left\langle 1-\left(\frac{|\mathbf{x}_I-\mathbf{x}_J|}{R}\right)^2\right\rangle. \tag{5.10}$$

The brackets $\langle ... \rangle$ denote the positive part, i.e., $\langle x \rangle = \max(0,x)$, and R is the filter radius which specifies the minimum allowed feature size. While this approach is heuristic, it produces results very similar to constrained local gradient methods in which

$$\left|\frac{\partial\phi}{\partial\mathbf{x}}\right| \le c \tag{5.11}$$

is enforced on the topology [26] The method is also very robust and is computationally efficient. It is shown below that filtering produces smoother part surfaces and eliminates mesh dependence.

5.3. Solution

The solution proceeds in the following steps:

1. Initialize displacement and levelset field to zero.
2. Compute equilibrium displacements.
3. Compute the sensitivities, A_I.
    a. Choose an arbitrary value for λ_2 and compute the initial A_I.
    b. Compute the updated ϕ_I field and apply filter if appropriate.
    c. Use the new ϕ_I to compute the material volume. Each element is subdivided by the surface $\phi(\mathbf{x}) = 0$. The region corresponding to $\phi(\mathbf{x}) > 0$ is tessellated to find the volume.
    d. Use bisection to compute an update value for λ_2.

e. Repeat steps (b) through (d) until the volume constraint is satisfied to a given tolerance.

4. Repeat steps 2 and 3 until the change in ϕ_I drops to a given tolerance.

5.4. Results

The algorithm in Section 5.2 was implemented in two and three dimensions in FlexFEM. In this section, test simulations are presented that demonstrate the usefulness of the method.

The first test simulation is in two dimensions and has rigid support on the left edge and a vertical force applied to the middle of the right edge. Figure 38 shows the results for $\alpha = 0.2$. By design, the higher order of $\overline{H}_1$ compared to $\overline{H}_2$ creates a penalty in the internal energy for intermediate values of ϕ. Consequently, the nodal values of ϕ tend to $-(\alpha - \gamma)$ and α producing the rough edges that are evident in Figure 38(a). Filtering the nodal sensitivities with a filter radius, R, of 0.4 produces the smoother result shown in Figure 38(b)

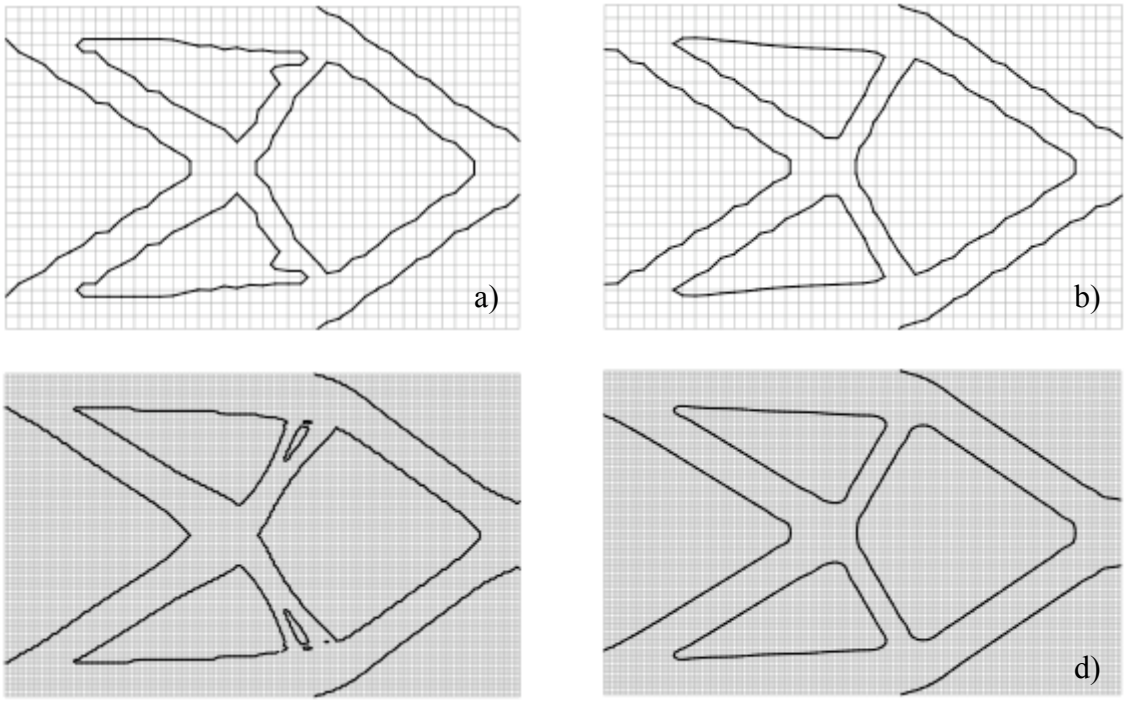

Figure 38: Two Dimensional Cantilever Structure.

Without filtering, as the mesh resolution increases (see Figure 38 (a) and (c)), the solution changes qualitatively. However, filtering eliminates the mesh dependency (see Figure 38 (b) and (d)) so that finer resolution produces smoother part surfaces but does not change the overall structure of the solution.

In many practical cases, such as when mating surfaces on structural members are prescribed, it may be more convenient to use a semi-conformal unstructured grid. Figure 39 shows the layout of an unstructured test problem where the mesh conforms to the loads and constraints. As in the first demonstration problem, the filter virtually eliminates any mesh dependence in the solution.

In this case, however, the unfiltered solution develops a *checker-board* instability in various parts of the design domain.

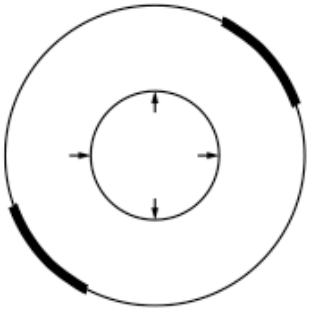

Figure 39: Layout for 2D Optimization on Unstructured Grid. Heavy Lines Indicate No Displacement and Arrows Indicate Tractions.

(a) Mean cell size: 0.01, no filter

(b) Mean cell size: 0.01, filter radius 0.04

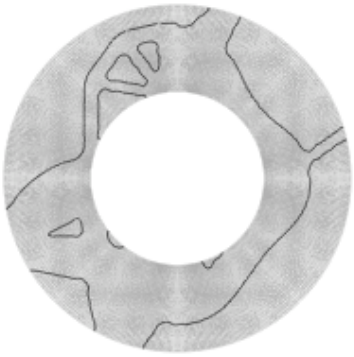

(c) Mean cell size: 0.005, no filter

Figure 40: Two Dimensional Optimization on an Unstructured Grid with Multiple Loads and Constraints.

The filtered and unfiltered solutions for the unstructured problem are qualitatively different, since the feature that is missing from the filtered case is below the feature size limit set by the filter radius, R. In fact, reducing the filter radius to 0.03 produces a topology with the missing feature.

6. 3D LASER ENGINEERED NET SHAPING™(LENS®)

One of the primary factors limiting the implementation of topological optimization has been the lack of a suitable method for manufacturing the optimized structures. While some optimized structures can be fabricated by conventional machining methods, many of the structures have features that are not accessible by milling, electro-discharge machining (EDM), lathe turning, or other conventional manufacturing methods. One of the primary limitations to conventional manufacturing methods is that they are subtractive meaning that material is removed from a large block of material to create the final part, however optimized parts often have features that cannot be accessed so the surrounding material cannot be removed. Because of these limitations, the team chose to utilize Laser Engineered Net Shaping™ (LENS®), a Sandia National Laboratories developed technology for additive manufacturing. However, LENS was a 2-1/2 D process and needed to be expanded to have full 3D capability in order to create optimized structures.

6.1. LENS Overview

LENS is process developed by Sandia National Laboratories and licensed for commercial use. The manufacturing process consists of a laser that is focused on a metal substrate creating a molten pool of metal. Metal powder is injected into this molten pool creating a bump. If the metal substrate is then moved around a work volume on a set of computer controlled axes, the process creates raised lines and arcs. These lines are drawn in close proximity to create a solid layer and then the laser is moved up by one layer thickness. Thus, line-by-line and layer-by-layer a part is created using only powdered metal. The final parts are fully dense material and have unique microstructure due to the rapid cooling of the melt pool. LENS deposited material has been shown to have up to 1.5 times the strength of wrought material, and because the strength increase was created through grain refinement, there is minimal accompanying loss of ductility. A schematic of the LENS system is shown in Figure 41 with the most significant process parameters labeled.

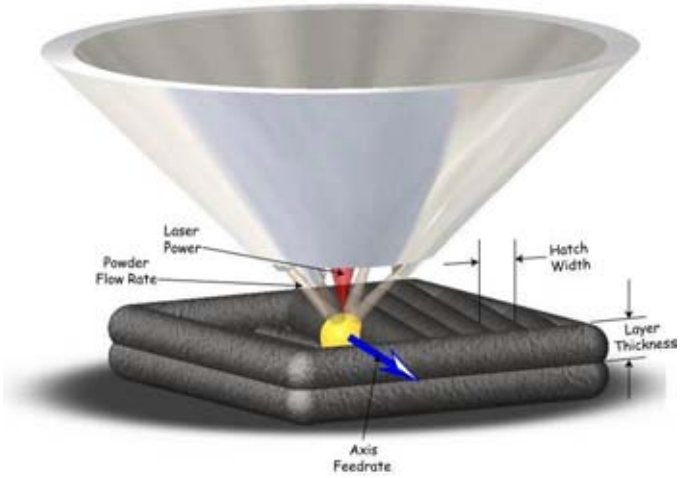

Figure 41. The LENS Process is Shown with the Most Significant Process Parameters Labeled.

6.2. LENS Machine Modifications

The LENS machine was originally built as a 2-1/2D machine meaning that the build process built a layer, moved up an incremental value, and then built the next layer. Because the LENS process requires that a melt pool first be created in existing material, there is a limited ability to create structures that angle outward, a condition called overhang. Overhang of up to 45˚ has been demonstrated by Sandia researchers in the past, but this requires optimum build conditions and part geometry. In most applications, overhanging structures are limited to 20˚ (from vertical). To be able to build generalized 3D structures, it would be necessary to change the machine and its controller to build in 3D.

6.2.1. Adding New Axes to the LENS Machine

In order to create a 3D capability for the LENS process, two additional axes had to be added to the existing machine configuration. The machine had two stacked, orthogonal, linear axes (labeled X and Y) underneath the part platen with a third mutually orthogonal linear axis (Z) mounted on the wall of the machine that moves the laser's focusing lens and the powder delivery system up and down above the part. Two rotational axes were designed, custom fabricated, and installed in the machine. These axes consist of an elevation axis (EL) that is mounted on the X axis and has its axis of rotation parallel to the machine's X axis. Stacked on top of the EL axis is an azimuth (AZ) axis that rotates around an axis parallel to the Z axis (when EL is at 0deg in the center of its travel). The EL axis can rotate +/- 95˚ from the vertical position and the AZ axis can rotate continuously in either direction. The 5 axes are shown installed in the LENS machine in Figure 42.

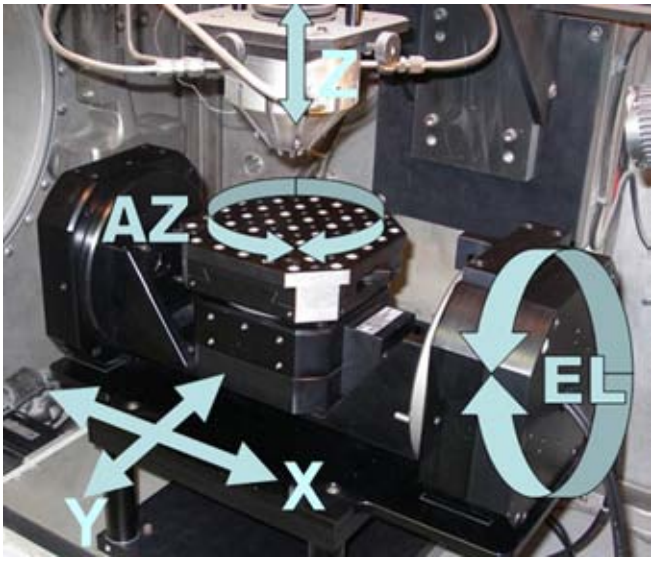

Figure 42. Elevation (EL) and Azimuth (AZ) Axes Were Added to the LENS Machine to Create a Fully 3D Capable Additive Manufacturing Process.

6.2.2. The LENS Controller and Inverse Kinematics

The additional axes in the LENS machine enable full 3D build capability, but they can make part programming much more difficult. In order to utilize the axes with the least pre-calculation, it is helpful put an inverse kinematic model into the controller. Using this model, the user can specify a point in the coordinate system of the part and a normal vector from that point and the system will determine the combination of axis positions that will achieve the desired results. To

develop this inverse kinematic model, the team developed the forward kinematics of the machine and then the related inverse kinematics transformations. Forward kinematics are used to convert from machine coordinates to part coordinates as follows: If each axis is set at a certain position, the forward kinematics will determine where the focal point of the LENS machine is and the normal vector of the nozzle in part coordinates. The inverse kinematic transformation is much more difficult, and is especially challenging because there are multiple solutions to most point/normal combinations. This is because the azimuth can usually be rotated 180 degrees and the elevation rotated from positive to negative (or vice-versa) and the same point/normal combination can be reached. This challenge was addressed by attempting to find the combination that required the least amount of motion to achieve when moving from the current position.

Another challenge in developing the inverse kinematics is developing the velocity terms. One would like to be able to go from point to point at a specified velocity. This requires the linear and rotary axes to move in concert and at varying speeds to maintain a constant velocity at some location in space. The velocity equations were developed and implemented.

The forward transformation [24] from machine coordinates (X, Y, Z, θ_{EL}, θ_{AZ}) to part coordinates (X_p, Y_p, Z_p).

$$\begin{bmatrix} X \\ Y \\ Z \\ 1 \end{bmatrix} = \text{Trans}(X,Y,Z)\,Rot(x,\theta_{El})\,Rot(z,\theta_{AZ})\,Trans[X_0,Y_0,Z_0] \begin{bmatrix} X_p \\ Y_p \\ Z_p \\ 1 \end{bmatrix} \tag{6.1}$$

Where

$$X_p = \sin\theta_{az}\sin\theta_{el}(Z) - \sin\theta_{az}\cos\theta_{el}(Y) - \cos\theta_{az}(X) - X_0 \tag{6.2}$$

$$Y_p = \cos\theta_{az}\sin\theta_{el}(Z) - \cos\theta_{az}\cos\theta_{el}(Y) + \sin\theta_{az}(X) - Y_0 \tag{6.3}$$

$$Z_p = \cos\theta_{el}(Z) - \sin\theta_{el}(Y) - Z_0 \tag{6.4}$$

$$U = \sin\theta_{el}\sin\theta_{az} \tag{6.5}$$

$$V = \sin\theta_{el}\cos\theta_{az} \tag{6.6}$$

$$W = \cos\theta_{el} \tag{6.7}$$

U, V, and W are the unit normal vectors along the X_p, Y_p, Z_p axes with values between 0 and 1.

For Sandia's LENS machine, the offset distances (in inches) utilized in the transformation are

$$X_0 = -5.9342$$

$$Y_0 = 5.6478$$

$$Z_0 = -9.375$$

The inverse kinematic transformations, adapted from [24] are as follows:

$$X = (X_P)\cos\theta_{az} - (Y_p)\sin\theta_{az} \tag{6.8}$$

$$Y = (X_p)\cos\theta_{el}\sin\theta_{az} + (Y_p)\cos\theta_{el}\cos\theta_{az} - (Z_p)\sin\theta_{el} + ELheight*(-\sin\theta_{el}) \tag{6.9}$$

$$Z = (X_p)\sin\theta_{el}\sin\theta_{az} + (Y_p)\sin\theta_{el}\cos\theta_{az} + (Z_p)\cos\theta_{el} + ELheight*(\cos\theta_{el} - 1) \tag{6.10}$$

For Sandia's LENS machine, the distance from the substrate surface to the center of rotation of the EL axis (ELheight) is 3.108". There are two cases for solutions. When the normal vector is not along the Z axis of the machine, there are two solutions for the rotational axes.

Case 1: W ≠ 1

$$\theta_{el} = \pm\cos^{-1}(W) \tag{6.11}$$

$$\theta_{az} = \tan^{-1}(\frac{U}{V}) \tag{6.12}$$

Where θ_{el} and θ_{az} both have multiple solutions of either (θ_{el}, θ_{az}) or (-θ_{el}, θ_{az} +180°). However, when the normal vector is along the Z axis of the machine, there is one solution and it is found by:

Case 2: U=V=0, *W*=1.

$$\theta_{el} = 0 \tag{6.13}$$

$$\theta_{az} = \tan^{-1}\left(\frac{U}{V}\right) \tag{6.14}$$

The solution is either (0, θ_{az}) or (0, θ_{az} +180°).

The inverse kinematics were utilized in the LENS machine with mixed success. The controller does an excellent job of determining the axis combination needed to achieve a certain point/normal combination. The velocity to get there is well controlled for linear axes, but still has some limitations for the rotary axes. Finally, there is a problem with the controller's software in that it moves to a starting location upon program start. Unfortunately, this move uses axis speeds that appear to be hard-coded into the software. The speeds require faster acceleration than the rotary axes are able to supply, so the system faults upon startup if the machine isn't started near its desired start location. This has been reported to the manufacturer of the axes and controller, but it has not been addressed by them and corrected.

6.3. 3D Process Planning for LENS

Sandia National Laboratories developed and patented the LENS process. As efforts to utilize LENS increased in complexity, it became apparent that a process planning system would be needed to create the part programs directly from part models. A system called Damocles was developed and licensed by Sandia. With the move to 3 dimensional, 5 axis motion, it was necessary to develop a new means of creating part programs. The problem of generalized 3D part programming is a difficult one for subtractive processes, and becomes even more complicated for additive manufacturing processes due to the need for material upon which to build. Additional complications include clearance for the nozzle, and the challenge of determining the best normal angle of the nozzle when joining multiple sections at intersections. Figure 43 shows that rotating a part so that the build direction is normal to the current build surface reduces complications with nozzle clearance and reduces the overhang of the current layer.

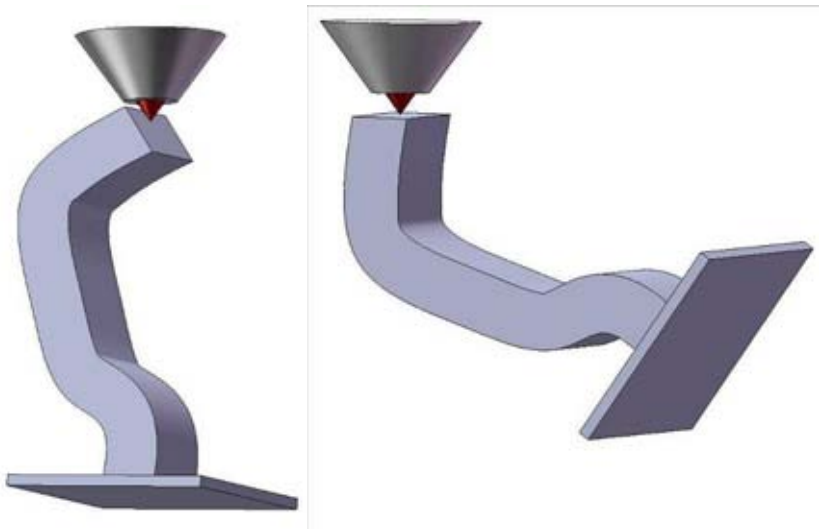

Figure 43. As LENS Builds Parts, Nozzle Clearance and Limited Overhang Can Cause Problems (left) Which Can Be Solved by Building the Part with the Laser Normal to a Chosen Build Surface(right).

Because of the limited monetary and people resources available to address the process planning challenge, the team chose to solve a more specific case that was applicable to the topology of many of the optimized structures that were being created by ATO and FlexFEM. The team noted that many of the parts consisted of thin "legs". One of the hardest parts of process planning for the generalized case is determining how to build the part by dividing it into layers. It would be nice to determine an axis up the middle of a part and then to slice the part into layers along that path. The team investigated multiple means of doing this including medial axis transformations and skeletonization, but elected to not pursue these because of the many difficulties that are encountered along the path. One of the chief difficulties is that surface features can disrupt the medial axis by creating small branches from the main axis. In attempts to reduce this miniature branching, many researchers have reduced the sensitivity of the transformation, but this leads to gaps at intersections with other intersecting geometry. The team decided that it would be most advantageous to utilize the user at this point. While it is very difficult for computers to determine the axis of an object, people are very adept at estimating where the best medial axis would reside. An example of user creation of medial axes is shown if Figure 44 for an optimized structure. The team developed a method in which the user imports the triangulated, optimized structure into a solid modeling program and then sketches 3D splines up the exterior surfaces of the part. Figure 44 shows a curved example part with a spline sketched on the surface. The team then developed code that steps along the spline adding nodes at the desired layer thickness for the LENS build parameters as shown in Figure 45. The software creates a plane at each of these points that is perpendicular to the spline. The intersection curve of the part and the plane are determined and this curve is used to create hatching and the machine code required to build the part. This software, named Damocles OE, has been shown to successfully plan the build coordinates for creating parts. The software has the capability to move all 5 axes simultaneously or to move the two rotary axes in between layers and then to build a flat layer at the each planned set of rotary axis positions. Several parts created using this software are shown in Figure 46.

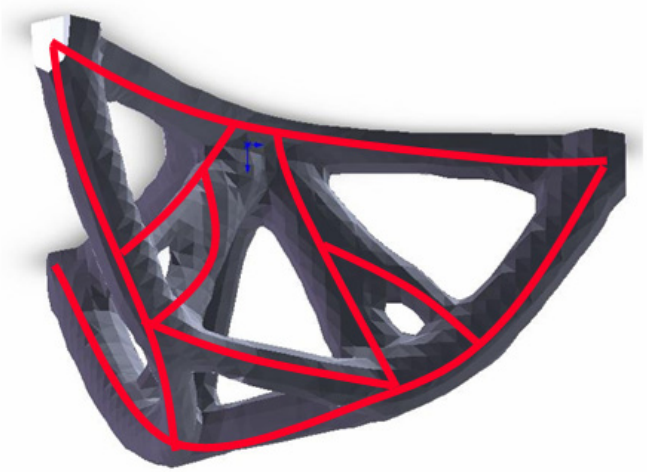

Figure 44. This optimized structure has medial axis splines that were sketched onto the surface of the part by a user.

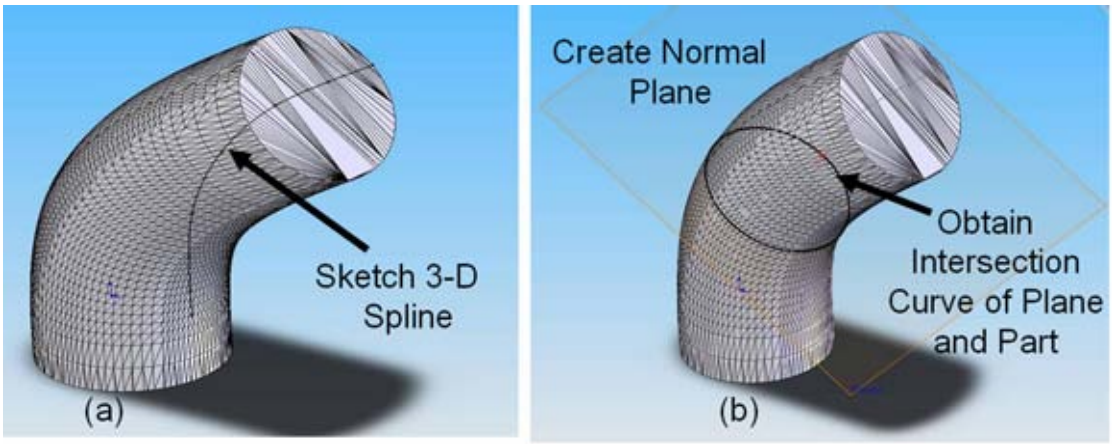

Figure 45. A part is shown with a spline sketched on the surface of the part (a) and with a normal plane and intersection curve (b).

Figure 46. Curved 3D Parts Built From 316 Stainless Steel Using the LENS Process.

7. BRINGING IT ALL TOGETHER

The team demonstrated the new topological optimization capability by selecting a real-world example, analyzing the original design, optimizing the structural topology, and then building the optimized structure using the 3D LENS capability. For this test, an optical lens housing, shown in Figure 47, was chosen. The lens housing requires that an open aperture be maintained and also has a minimal mass to begin with, making the optimization of this housing not be intuitive. The lens housing could have its mass reduced, but primarily needed to have its mass redistributed to prevent lens distortion under loading. The optical lens is supported kinematically by a wave spring that rests on the bottom ledge of the mount. When the retaining ring is tightened, the ring puts a distributed load on the lens. The lens transmits this load to the wave spring at 3 locations which transmits the load to the ledge. Under load, the housing deflects and permits distortion of the lens.

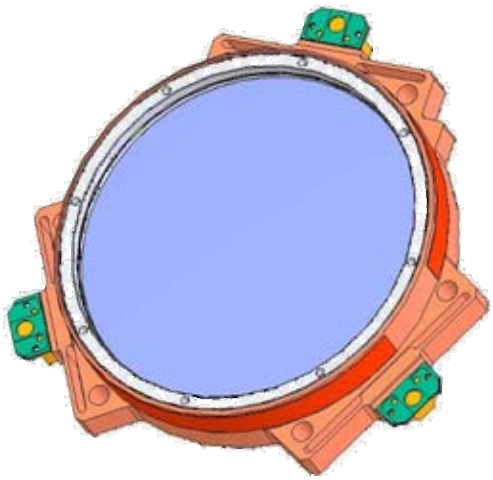

Figure 47. Lens Housing Test Case.

7.1. Finite Element Analysis of Current Design

As discussed previously, the lens housing was selected as a potential demonstration case for weight reduction through the application of numerical optimization procedures currently under development. As a first step in this process, a conventional finite element analysis of the current lens housing design was performed using the commercial finite element package, Abaqus/Standard.

The finite element mesh generated using Abaqus/CAE is shown in Figure 48. In finite element modeling of three dimensional components, improved accuracy for a given element size is achieved using hexahedral (brick) elements as compared to tetrahedral elements. For complex shapes, however, meshing algorithms are unable to generate meshes using hexahedral elements. Abaqus/CAE provides a capability to partition a component into regions that can be meshed with hexahedral elements. As shown in Figure 48, partitioning was used to obtain hexahedral element meshes in some parts of the structure. In other regions, however, meshing with tetrahedral elements was required. For both hexahedral and tetrahedral elements, quadratic interpolation was selected. The hexahedral elements have 20 nodes and the tetrahedral elements have 10 nodes. The mesh shown in Figure 48 has a total of 100,915 elements. This mesh density provides

reasonably accurate predictions of global stress levels. Prediction of detailed stress fields in the vicinity of stress concentrations, however, would require refined mesh density in these regions. Since the primary objective of the current analysis is to identify low stress regions where material can be removed for weight savings, it is believed that the mesh shown in Figure 48 is adequate for this purpose.

The lens housing is supported by mounting brackets that are bonded to three pads at the three flexures in the lens housing. This support condition was simulated by constraining the nodes on these faces in all three directions. The loads consisted of three axial concentrated forces at 120° intervals along the perimeter of the lens support region. These forces are due to contact with a wave spring that supports the lens. Since the orientation of the wave spring is uncertain, two load cases were considered. In case 1, these forces are taken to be aligned with the mounting brackets. In case 2, the forces are applied midway between the mounting brackets. The material was taken to be 7075-T73 aluminum.

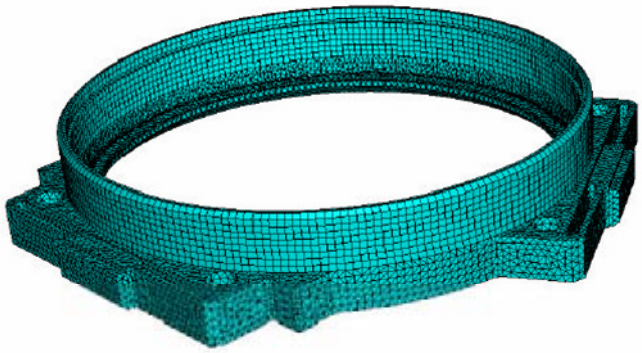

Figure 48. Finite Element Mesh of Lens Housing.

The results of the finite element analysis are shown in Figure 49 which are von Mises stress contour plots for the two different load cases. Since the objective of this analysis is to identify low stress regions for potential material removal, the von Mises stress contour limit was set to 50 MPa, well below the nominal yield stress of 480 MPa. For both cases, two regions of high stress are observed. In the regions where the concentrated forces are applied, high stresses are observed. These high stresses, however are due to stress concentration effects associated with point loading in the finite element model. In the actual component, this load is due to contact with the wave spring. The actual contact region has finite dimensions and would result in contact stresses much lower than that obtained when the contact force is modeled as a point loading. If details of the stresses in these regions are required, a more detailed analysis of the wave spring contact region is needed. The other region of high stress levels in both cases is in the vicinity of the flexure supports. Comparing the stress fields in this region for cases 1 and 2, it is clear that the location of the load application points do not significantly affect the stresses near the flexure supports. Since the stresses in this region are relatively high, it is expected that optimization of this structure by material removal would not significantly alter the design in this region. Furthermore, since the flexure geometry was likely selected based on other considerations such as dynamic effects, it is expected that changing the design of this region would be undesirable.

The cylindrical body of the lens housing is observed to experience relatively low stress for both cases. For case 1, the load path is seen to be directly from the load application point through the flexure supports into the mounting brackets. As a result, the stresses in the cylindrical body

between the mounting brackets are extremely low. For case 2, where the load is applied midway between the mounting brackets, the stresses in the cylindrical body between the mounting brackets are higher than those in case 1 but are still relatively low.

The results of these analyses indicate that since much of the material in the lens housing is stressed at levels well below the yield stress, significant weight savings are possible. It is anticipated that application of the numerical optimization currently under development could identify a minimum weight topology that could be used to guide redesign of this component.

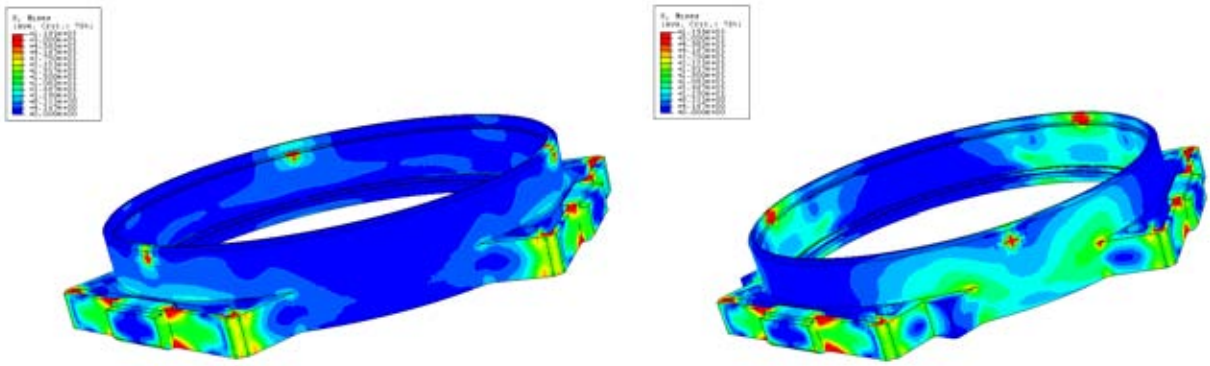

Figure 49. Von Mises Stress Contours for Case 1 (left) and Case 2 (right).

7.2. Optimization of Lens Housing

The housing was optimized using both ATO and FlexFEM. The 3D optimization capability in FlexFEM was applied to the optical lens housing. Figure 50 shows design envelope and the resulting topology painted with axial stress levels. The simulation consists of an unstructured partially conformal grid that captures the loaded surfaces. Loads are applied at six equally spaced regions within the lip of the ring and the surfaces directly above the loads are held fixed. The filter radius used for this simulation produces the three-ribbed solution shown in Figure 50. If the filter radius is decreased in order to allow smaller features, the number of ribs in the solution increases.

Similarly, the optimized housing as defined by ATO is shown in Figure 51(left). Using the LENS process and the results of the ATO optimization, an optimized lens housing was created from 316 stainless steel. It is evident that the two independently developed solutions match quite well, suggesting that the results represent a truly optimized housing. There are some differences such as the number of ribs on the back of each vertical tab. These differences were caused by input parameters such as the filter radius which sets a minimum feature size. Additionally, the ATO model was probed for its sensitivity to both the number of iterations and the number of finite elements used in the solution. The results are shown in Figure 52. A lower number of iterations caused reduced feature definition (Figure 52 a, c, e) and a reduced element size caused a more continuous structure (Figure 52f). This is most evident in the “flying buttresses” supporting the vertical tabs. The interior structure of these buttresses goes from individual spokes to a continuous flat plate as the element size decreases.

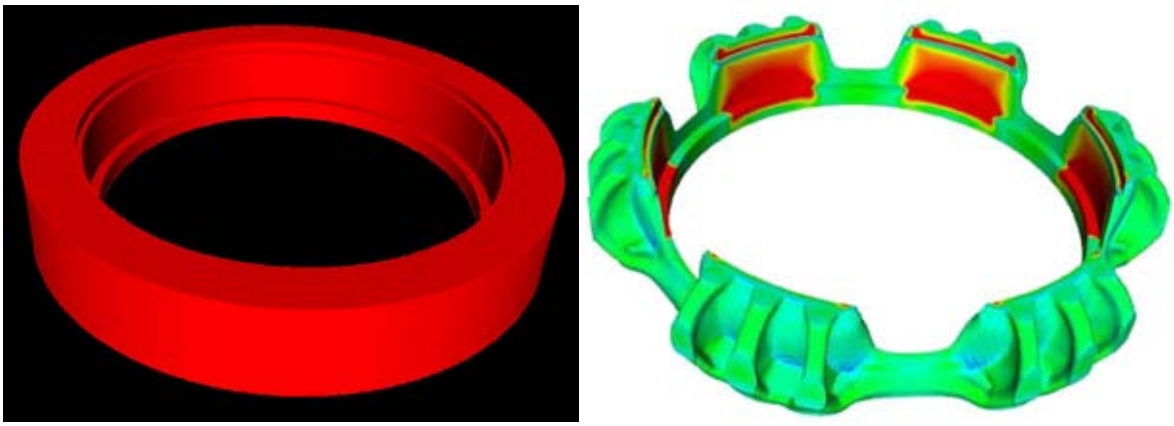

Figure 50: FlexFEM Design Envelope (left) and 3D Optimized Lens Housing (right).

Figure 51. ATO Optimized 3D Lens Housing (left) and LENS Manufactured Housing (right).

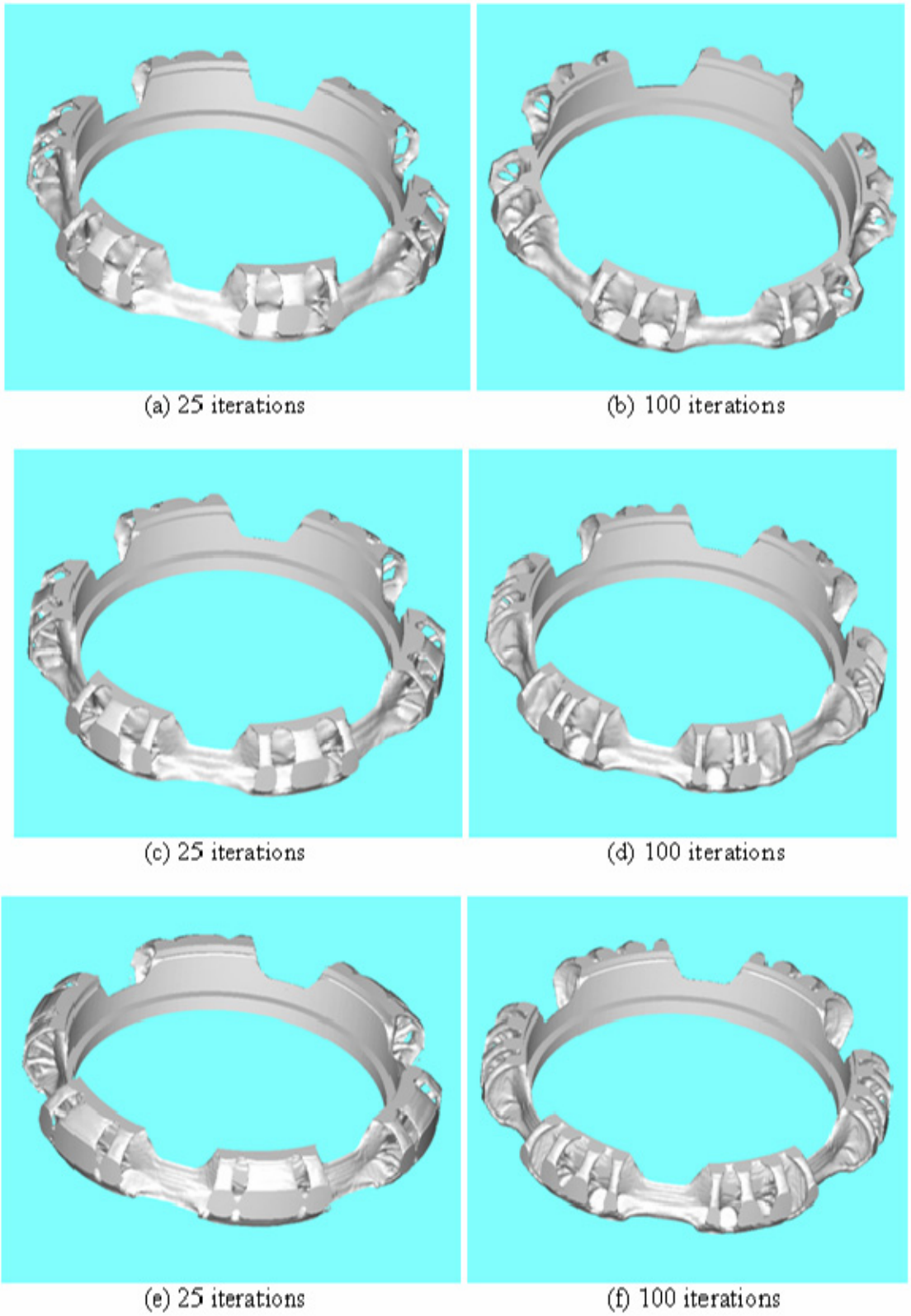

Figure 52. The ATO Results Show the Effects of Different Mesh Densities and Iteration Counts. The mesh densities shown (for a 1/12th symmetry model) are 6600 elements (a&b), 17,442 elements (c&d), and 100,608 elements (e&f).

8. CONCLUSIONS

The Titanium Cholla LDRD team has the potential to have a significant impact on the design community by providing verified, robust, generalized, 3D optimization solution methods and a manufacturing method capable of creating the optimized structures. The team developed new analytically optimized 3D structures to verify the capabilities of the finite element based optimization methods. New capabilities in optimization included the move from 2D to 3D, the development of excluded regions that are exempt from optimization (for bolt holes, open apertures, etc.), and methods of recording these structures in a format that can be used to create manufactured parts. The manufacturing team developed a 3D capability for the Laser Engineered Net Shaping™ (LENS®) process and then created a novel 3D process planning capability. Using these two developments, the team built numerous 3D structures in fully functional engineering metals. Finally, the team demonstrated the whole capability working together by optimizing a real-world 3D test case and building the optimized structure using LENS. The results of this LDRD have the potential to save significant amounts of time and money as designers attempt to create the lightest, strongest structures for many applications including aerospace.

9. REFERENCES

1. Michell, A. G. M., "Limits of economy of material in frame-structures", Philosophical Magazine, 6, 589-597, 1904.
2. Bendsoe, M. P., and Kikuchi, N., Generating optimal topologies in structural design using a homogenization method. *Computer Methods in Applied Mechanics and Engineering*, 71**,** 197-224, 1988.
3. Bendsoe, M. P. and Sigmund, O., "Topology Optimization," Springer-Verlag, 2004.
4. Xie, Y. M. and Steven, G. P., "A simple evolutionary procedure for structural optimization," Computers and Structures, 49, 885-896, 1993.
5. Xie, Y. M., and Steven, G. P., "Evolutionary structural optimization," Springer, London, 1997.
6. Abaqus Analysis User Subroutine Reference Manual, version 6.6, Abaqus, Inc., Providence, RI, 2006.
7. Nair, A., Demircubuk, M., Dewhurst, P. and Taggart, D., "Evolutionary techniques for identifying minimum weight topologies and for the suppression of global instabilities," ABAQUS Users Conference, May 2005.
8. Nair, A., Taggart, D. and Dewhurst, P. "A novel evolutionary topology optimization algorithm," in preparation, 2006.
9. Press, W. H., Flannery, B., P., Teukolsky, S., A., and Vetterling, W. T., "Numerical recipes in FORTRAN 77: The art of scientific computing," Cambridge University Press, 1992.
10. Chan, A. S. L., "The design of Michell optimum structures," Report No. 142, College of Aeronautics, Cranfield UK, December 1960.
11. Johnson, W., Chitkara, N. R., Reid, S. R., and Collins, I. F., "The displacement field and its significance for certain minimum weight two-dimensional frames," *International Journal of Mechanical Sciences*, 13, 547, 1961.
12. Hemp, W.S. 1958: Theory of structural design. *Cranfield College of Aeronautics* Report No. 115
13. Prager, W. 1958: A problem of optimal design. *Proc. UTAM.* Warsaw
14. Rozvany, G.I.N. 1996: Some shortcomings of Michell's truss theory. *Struct. Optim.* 12, 244-250
15. Dewhurst, P. 2005: A general optimality criterion for strength and stiffness of dual-material-property structures. *Int. J. Mech. Sci.* 47, 293-302.
16. Lewinski, T. 2004: Michell structures formed on surfaces of revolution. *Struct. Multidisc. Optim.* 28, 20-30
17. Hemp, W.S. 1973: *Optimum structures.* Oxford: Clarendon

18. Taggart, D. G. and Dewhurst, P., 2007: An efficient finite element based topology optimization procedure for the identification of minimum weight structures, in preparation.

19. Lorensen, W. and Cline, H. E., "Marching Cubes: A High Resolution 3D Surface Construction Algorithm", Computer Graphics - Proceedings of SIGGRAPH '87, Vol. 21, No. 4, pp. 163-169, 1987.

20. Srithongchai, S., Demircubuk, M. and Dewhurst, P. A theoretical and experimental investigation of a family of simply-supported beams. Int. J. Mechanical Sciences 45 (2003) 37-55.

21. Kozlowski, W. and Mroz, Z. Optimal design of disks subject to geometric constraints. Int. J. Mechanical Sciences 12 (1970) 1007.

22. Demircubuk, M. Design and Manufacture of Optimum Product Structures, Ph.D. Dissertation, University of Rhode Island, 1985.

23. Mongdon, C.E. Equilateral triangle on the surface of a sphere. Internal report, Rice University, 2004 (http://math.rice.edu/~pcmi/sphere/gos4.html)

24. Lei, W. T. and Hsu, Y. Y. (2003) “Error Measurement of Five-Axis CNC machines with 3D probe-ball”, Journal of Materials Processing Technology, vol. 139, issue 1-3, pp. 127-133.

25. Belytschko, T., Xiao, S. P., Parimi, C., Topology optimization with implicit functions and regularization. Int. J. for Numerical Methods in Engineering, vol 57, pp. 1177-96, 2003.

26. Sigmund, O. and Petersson, J., Numerical instabilities in topology optimization: A survey on procedures dealing with checkerboards, mesh-dependencies and local minima. Structural Optimization, vol 16, pp. 68-75, 1998.

DISTRIBUTION

External Mailings

2 University of Rhode Island
College of Engineering
Attn: Peter Dewhurst
Gilbreth Hall
Kingston, RI 02881

Sandia National Laboratories – Internal Mailings

1	MS0378	Thomas Voth	1433
4	MS1245	David Gill	2455
1	MS1245	Clinton J Atwood	2455
1	MS1322	Joshua Robbins	1435
1	MS0899	Technical Library	9536 (electronic copy)
1	MS0123	Donna Chavez, LDRD	1011